

Why Sample Space Matters: Keyframe Sampling Optimization for LiDAR-based Place Recognition

Nikolaos Stathoulopoulos, Vidya Sumathy, Christoforos Kanellakis and George Nikolakopoulos

Abstract—Recent advances in robotics are pushing real-world autonomy, enabling robots to perform long-term and large-scale missions. A crucial component for successful missions is the incorporation of loop closures through place recognition, which effectively mitigates accumulated pose estimation drift. Despite computational advancements, optimizing performance for real-time deployment remains challenging, especially in resource-constrained mobile robots and multi-robot systems since, conventional keyframe sampling practices in place recognition often result in retaining redundant information or overlooking relevant data, as they rely on fixed sampling intervals or work directly in the 3D space instead of the feature space. To address these concerns, we introduce the concept of sample space in place recognition and demonstrate how different sampling techniques affect the query process and overall performance. We then present a novel keyframe sampling approach for LiDAR-based place recognition, which focuses on redundancy minimization and information preservation in the hyper-dimensional descriptor space. This approach is applicable to both learning-based and handcrafted descriptors, and through the experimental validation across multiple datasets and descriptor frameworks, we demonstrate the effectiveness of our proposed method, showing it can jointly minimize redundancy and preserve essential information in real-time. The proposed approach maintains robust performance across various datasets without requiring parameter tuning, contributing to more efficient and reliable place recognition for a wide range of robotic applications.

Index Terms—Global Localization, Place Recognition, Loop Closure, Keyframe Sampling, Optimization.

I. INTRODUCTION

Simultaneous Localization and Mapping (SLAM) is a cornerstone of modern robotics, with applications ranging from self-driving vehicles [1] to autonomous subterranean inspection missions [2], and search and rescue operations in challenging environments [3], [4]. As highlighted throughout the literature [5]–[7], the key components for successful SLAM in long-term and large-scale missions are the accurate pose estimation in the front-end and the addition of loop closures, through place recognition (PR) in the back-end, which helps to mitigate any accumulated errors during pose estimation. For the front-end, many efficient algorithms have been proposed to provide robust estimation using dynamic data structures [8]. Additionally, integrating and fusing extra sensors is a popular approach to enhance the resilience of the system [9]. Focusing on the back-end, global localization, particularly through place recognition, has gained significant

The Authors are with the Robotics and AI Group, Department of Computer, Electrical and Space Engineering, Luleå University of Technology, 971 87 Luleå, Sweden. Corresponding Author's e-mail: niksta@ltu.se

This paper is supported by code and demonstration files, available at <https://github.com/LTU-RAI/opt-key.git>.

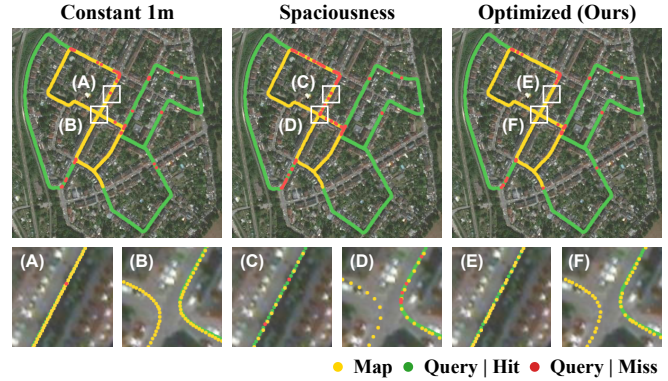


Fig. 1. An example on KITTI Odometry 00 sequence. Our approach outperforms other sampling methods, like constant interval and spaciousness-based adaptive techniques. The top figures show an overview of the retrieval performance, while the bottom figures highlight specific instances. Yellow: map samples, green: correctly classified query samples, red: false matches.

attention in recent years [10]–[12], with numerous learning-based architectures being introduced annually. Advances in computational resources have enabled the development of increasingly complex algorithms [13], more evident in the realm of learning-based approaches, where the number of layers or parameters in a network continues to grow. However, a gap persists between optimizing performance and meeting real-time deployment requirements, especially for mobile robots with limited computational power and memory, as noted in [14]. Moreover, in multi-robot systems, minimizing the information exchanged between agents is critical due to the inherent communication overhead [15], [16], with popular solutions utilizing hierarchical structures through semantic [17] and topological information [18].

The current literature often assesses place recognition performance in densely sampled public datasets, where a large number of samples can artificially enhance performance. However, this high-density sampling results in significant challenges for mobile robots in global localization tasks, as they must compare query samples with an ever-expanding map database. In practice, conventional methods typically involve setting a fixed interval for keyframe sampling based on distance [19]–[24]. However, this approach may lead to the retention of redundant information or the omission of relevant data. Additionally, determining an appropriate fixed interval is challenging, as it depends on both the environment and the feature extraction framework used. Developing an effective keyframe sampling strategy for place recognition is further complicated by the non-causal nature of requiring future query samples, which makes balancing the retention

of useful data and the exclusion of redundancy in dynamic environments difficult.

A. Related Work

We categorize the keyframe sampling techniques in the literature into two types: those used in vision-based systems and those used in LiDAR-based systems. Our focus lies on the optimization of the sampling process, rather than solely on their application. This emphasis is due to the lack of methods specifically addressing keyframe sampling for place recognition in the existing literature, as most techniques target sampling for pose graph optimization.

1) *Keyframe sampling in vision-based systems:* The work in [25] introduced a keyframe selection method, which focused on improving visual SLAM criteria by identifying higher quality and more meaningful keyframes. Their approach incorporates a two-criterion evaluation window, considering image-quality and semantic content scores to prioritize keyframes for subsequent place recognition tasks. In contrast, [26] presented a keyframe-based visual SLAM method for globally consistent 3D reconstruction, utilizing keyframes for loop closure and bundle adjustment through local and global pose optimization. The transition from semantic-based keyframe selection to global consistency emphasizes the importance of diverse criteria for keyframe relevance in different SLAM tasks. Conversely, [27] proposed a visual odometry technique based on pose adjustment with keyframe matching, employing keyframes primarily for local adjustments. This shift from global to local optimization strategies highlights the flexibility in keyframe usage across different SLAM approaches. Additionally, the work in [28] introduced a dynamic strategy for keyframe selection using a PD controller in visual SLAM systems, dynamically determining when to add keyframes based on feedback from view changes. This adaptation-based approach underscores the need for real-time responsiveness in keyframe selection. Furthermore, in [29] it was utilized the keyframe concept to maintain a bounded-size optimization window for real-time operation in visual SLAM, selecting keyframes based on a heuristic approach, considering the ratio between matched points to detected points. Their method bridges the gap between dynamic and static keyframe selection strategies, offering a compromise between responsiveness and computational efficiency. An extension to a monocular visual-inertial SLAM system was proposed in [30], managing keyframes for both local and global optimization. This integration of visual and inertial data showcases the importance of multimodal fusion in keyframe management. Lastly, [31] presented a visual-inertial odometry method, tailored for autonomous vehicles, introducing a keyframe selection strategy adaptable to various conditions, using principles based on feature matching, spatial position difference, and yaw difference.

2) *Keyframe sampling in LiDAR-based systems:* In LiDAR-(Inertial) Odometry, keyframe sampling often relies on fixed intervals, either based on Euclidean distance [19] or time [20]. These keyframes serve various purposes, including local map maintenance, loop closure, and global pose

optimization. Recent advancements, such as those in [32] and [33], dynamically adapt the keyframe sampling interval based on the spaciousness of the environment, optimizing the process of scan-to-submap matching using techniques like k -Nearest Neighbor (k -NN) search. However, a drawback is the requirement for manual tuning of spaciousness thresholds to adjust the fixed distance sampling interval. Entropy-based strategies, like the one proposed in [34], offer an alternative approach to keyframe selection in LiDAR odometry and mapping, by leveraging information theory. This method determines keyframe generation instances to enhance local map updates and front-end point cloud matching. Thus, the keyframe buffer is updated based on feature point transformations and the calculation of Fisher information and information entropy. Nevertheless, the main drawback is its limited adaptability, as the information change threshold may need adjustment for different environments. In [35], the keyframe selection relies on similarity in displacement vectors, aiming to balance computational cost and map completeness. Keyframes are extracted and added to a local sliding window, with new keyframes generated when the current frame exceeds a specified distance threshold. This approach typically maintains a limited number of keyframes in the sliding window for efficient local pose optimization. Several LiDAR-based place recognition approaches adopt fixed distance intervals for keyframe extraction [21], [22], focusing primarily on front-end odometry modules without considering keyframe accumulation over time. Conversely, in [36], a place recognition method for loop closure incorporates a 3D bag of words [37], with a keyframe selection strategy for vocabulary building. The method employs LinK3D [38] features and avoids redundant information by setting new keyframes based on matching between current frames and reference keyframes.

B. Contributions

In this article, we introduce a novel optimization-based approach to keyframe sampling, aimed at improving the efficiency of global localization tasks like place recognition for loop closures and multi-robot map merging [39], both critical for enhanced situational awareness. Inspired by video summarization techniques, our method optimizes keyframe extraction from LiDAR sequences, streamlining global localization without compromising performance.

To achieve this, we propose an adaptive sliding window framework that eliminates redundant keyframes while preserving essential information. This framework avoids manual threshold tuning and improves adaptability across different environments. Our approach quantifies redundancy and evaluates the correlation between keyframe descriptors and pose changes within each sliding window. By analyzing the correlation matrix and transforming descriptors along their principal components, we ensure critical information is preserved while minimizing memory usage. This keyframe sampling strategy is formulated as an optimization problem that balances redundancy and information preservation, ensuring efficient place recognition. A snapshot of the results

of our keyframe sampling method is illustrated in Fig. 1, utilizing the KITTI dataset. Finally, the contributions of this article, can be summarized as follows:

- **Does sample space matter?** We raise critical questions about sampling strategies in place recognition, highlighting the limitations of fixed-interval methods and their performance loss, and present the results through an evaluation study.
- **Redundancy and Information Preservation:** We introduce the concepts of *redundancy minimization* and *information preservation* within the hyper-dimensional descriptor space, demonstrating their efficacy on both learning-based and handcrafted descriptors.
- **Optimizing keyframe sampling for PR:** We introduce a novel optimization framework for LiDAR-based place recognition, minimizing redundancy while preserving essential information in keyframe sampling, thereby reducing memory overhead without compromising retrieval performance, crucial for real-time deployment on resource-constrained platforms.
- **Adaptability and Robustness:** The proposed approach is able to adapt to various environments, delivering robust performance without the need for manual parameter tuning, unlike fixed threshold methods.

We present our approach in detail, demonstrating its effectiveness through an extensive evaluation and comparative analysis against existing sampling methods. The primary objective is to advance global localization techniques for more efficient and practical robotic applications in diverse real-world scenarios, while addressing the gap in existing literature, where keyframe sampling methods primarily focus on global pose optimization rather than place recognition.

C. Outline

The remainder of this article is organized as follows. Section II introduces the fundamental concepts of global localization, which are essential for understanding the problem formulation presented in Section III. Section IV then details the two main concepts underlying our proposed optimization method, followed by a description of the optimization solution and implementation details in Section V. The experimental evaluation setup is outlined in Section VI, with the results presented in Section VII. Finally, the article concludes with a brief discussion in Section VIII, and wraps up with the concluding remarks in Section IX.

II. PRELIMINARIES

The *global localization* problem [10] in robotics is defined as the estimation of the state or pose of a robot, denoted as $\mathbf{x}_t \in \mathbf{X}$, within a known map \mathbf{M} , using a sensor observation \mathbf{z}_t . Mathematically, this can be formulated as a Maximum Likelihood Estimation (MLE) problem [40], given by:

$$\hat{\mathbf{x}}_t = \arg \max_{\mathbf{X}} p(\mathbf{z}_t | \mathbf{x}_t, \mathbf{M}). \quad (1)$$

Here, $\mathbb{X} \equiv \mathbf{X}$ represents the pose space and $p(\mathbf{z}_t | \mathbf{x}_t, \mathbf{M})$ is the likelihood function, representing the probability of

observing \mathbf{z}_t , given the state \mathbf{x}_t and the known map \mathbf{M} . Unlike *local pose tracking*, *global localization* lacks prior pose information, expanding the search space significantly. To manage this complexity, a retrieval-based approach is adopted, commonly through *place recognition*. We define the keyframes $\mathbf{K} = \{\mathbf{k}_1, \mathbf{k}_2, \dots, \mathbf{k}_N\}$ as triplets, consisting of a pose coupled with a submap (typically represented by a single LiDAR scan) and a descriptor. The keyframe poses are denoted as $\mathbf{X} = \{\mathbf{x}_1, \mathbf{x}_2, \dots, \mathbf{x}_N\}$, where $\mathbf{x} \in SE(3)$, while the corresponding keyframe submaps are represented by $\mathbf{Z} = \{\mathbf{z}_1, \mathbf{z}_2, \dots, \mathbf{z}_N\}$, where $\mathbf{z} \in \mathbb{R}^{L \times 3}$, L is the amount of points within a LiDAR scan and $N \in \mathbb{N}$ is the total number of keyframes describing the given map. The map, $\mathbf{M} = \{\mathbf{m}_1, \mathbf{m}_2, \dots, \mathbf{m}_N\}$, where $\mathbf{m} \in \mathbb{R}^{L \times 3}$, can be considered as a collection of the observations \mathbf{z} properly transformed to the static world frame from the non-static local sensor frame. As a common practice in the literature [10], the map representation is transformed into descriptive vectors $\mathbf{D} = \{\mathbf{d}_1, \mathbf{d}_2, \dots, \mathbf{d}_N\}$ through a feature extraction process. Here, $\mathbf{d} \in \mathbb{R}^M$ and $M \in \mathbb{N}$ is the feature dimensionality defined by the given descriptor extraction pipeline. This process, denoted as a function $F(\mathbf{z}_i) = \mathbf{d}_i, \forall \mathbf{z}_i \in \mathbf{Z}$, is typically either learning-based [41], [42] or handcrafted [43], [44]. These descriptive vectors contribute to efficient matching and querying in subsequent stages of the *place recognition* pipeline. Thus, the keyframes can be succinctly denoted as:

$$\mathbf{K} = \left\{ \underbrace{(\mathbf{x}_1, \mathbf{z}_1, \mathbf{d}_1)}_{\mathbf{k}_1}, \underbrace{(\mathbf{x}_2, \mathbf{z}_2, \mathbf{d}_2)}_{\mathbf{k}_2}, \dots, \underbrace{(\mathbf{x}_N, \mathbf{z}_N, \mathbf{d}_N)}_{\mathbf{k}_N} \right\} \quad (2)$$

The map \mathbf{M} can now be represented by the descriptors \mathbf{D} , thus, Eq. (1) becomes:

$$\hat{\mathbf{x}}_k = \arg \max_{\mathbf{X}} p(\mathbf{z}_k | \mathbf{x}_k, \mathbf{D}) \quad (3)$$

where $\mathbf{X} \subset \mathbb{X}$ is the discrete subset of the pose space. The size of the keyframe list, N , determines the constrained search space $|\mathbf{X}| \ll |\mathbb{X}|$. The retrieval-based approach bounds the estimated pose within a range of the true pose, $\delta_{min} \leq \|\mathbf{x}_k - \hat{\mathbf{x}}_k\|_2 \leq \delta_{max}$, with an accuracy influenced by the descriptor extractor's quality.

The sampling interval between keyframes significantly impacts map representation and retrieval performance, as demonstrated in Fig 1 and during the experimental evaluation in Section VII. Dense keyframe sampling increases the likelihood of successful retrieval, since multiple keyframes can lead to a matching candidate. However, dense and unfiltered sampling may introduce redundant or noisy samples due to agile motions of the robot or other environmental disturbances. Moreover, enlarging the keyframe list can result in higher computational loads during querying and increased memory allocation, especially in large scale environments or long term missions. Therefore, finding a balance between keyframe density and list size is essential to optimize retrieval accuracy and computational efficiency in *global localization* tasks.

III. PROPOSED PROBLEM FORMULATION

Let us consider a keyframe set $\mathbf{K}_M = \{\mathbf{X}_M^T, \mathbf{Z}_M^T, \mathbf{D}_M^T\}$ that represents the environment, a query set $\mathbf{K}_Q = \{\mathbf{X}_Q^T, \mathbf{Z}_Q^T, \mathbf{D}_Q^T\}$ and a descriptor extraction process $F: \mathbb{R}^3 \rightarrow \mathbb{R}^M$, then, the retrieval task for the whole query set can be defined as:

$$\underset{\bar{\mathbf{K}}=\{\mathbf{k}_j:\mathbf{k}_j\in\mathbf{K}_M\}}{\text{minimize}} \sum_{(\mathbf{k}_i,\mathbf{k}_j)\in\mathbf{K}_M^Q} f_o(\mathbf{k}_i, \mathbf{k}_j), \quad (4)$$

$$\text{subject to } \forall \mathbf{k}_i \in \mathbf{K}_Q, \bar{\mathbf{K}} \subseteq \mathbf{K}_M, |\bar{\mathbf{K}}| = |\mathbf{K}_Q| \neq 0$$

where $\mathbf{K}_M^Q = \mathbf{K}_Q \times \mathbf{K}_M = \{(\mathbf{k}_i, \mathbf{k}_j) : \mathbf{k}_i \in \mathbf{K}_Q, \mathbf{k}_j \in \mathbf{K}_M\}$ is the space of all the possible combinations between the query and map set, and $f_o(\cdot)$ is the retrieval function given by the corresponding feature extraction framework F . A common function used is the M -dimensional norm between two descriptors $f_\delta(\mathbf{d}_i, \mathbf{d}_j) = \|\mathbf{d}_i - \mathbf{d}_j\|_M$, or a similarity measure like $f_\sigma(\mathbf{d}_i, \mathbf{d}_j) = 1/(1 + \|\mathbf{d}_i - \mathbf{d}_j\|_M)$. Notably, given the function $f_o(\cdot)$, it's essential to specify the sign of the function to align with the definition of minimization.

The minimization problem defined in Eq. (4) aims to find the subset $\bar{\mathbf{K}} \subseteq \mathbf{K}_M$ that contains the corresponding nearest candidate for every \mathbf{k}_i in the query set \mathbf{K}_Q . To reduce the search space of the map keyframes \mathbf{K}_M , we propose the following formulation:

$$\underset{\substack{\mathbf{K}_M^* \subseteq \mathbf{K}_M, \\ \bar{\mathbf{K}} \subseteq \mathbf{K}_M^*}}{\text{arg min}} g_o(\mathbf{K}_Q, \mathbf{K}_M) = \underset{\substack{\mathbf{K}_M^* \subseteq \mathbf{K}_M, \\ \bar{\mathbf{K}} \subseteq \mathbf{K}_M^*}}{\text{arg min}} \sum_{(\mathbf{k}_i,\mathbf{k}_j)\in\mathbf{K}_M^Q} f_o(\mathbf{k}_i, \mathbf{k}_j), \quad (5)$$

where \mathbf{K}_M^* is the minimum-cardinality subset of \mathbf{K}_M over which the minimization problem converges to the same optimum set $\bar{\mathbf{K}}$, as in the original formulation in Eq. (4):

$$\mathbf{K}_M^* = \underset{\mathbf{K} \subseteq \mathbf{K}_M}{\text{arg min}} |\mathbf{K}| \quad (6)$$

$$\text{subject to } \underset{\bar{\mathbf{K}} \subseteq \mathbf{K}_M^*}{\text{arg min}} g_o(\mathbf{K}_Q, \mathbf{K}_M^*).$$

To solve the aforementioned combinatorial optimization problem that refers to a minimum-cardinality problem, we must consider both sets \mathbf{K}_M and \mathbf{K}_Q . However, this approach is impractical as our objective is to dynamically minimize the size of the map keyframe set \mathbf{K}_M in real-time, before its utilization with the query set \mathbf{K}_Q . Determining the contribution of a keyframe to the optimization process is largely based upon knowledge of the target query set, thus, the system lacks causality as it necessitates future inputs. Furthermore, the problem falls within the NP-hard class due to its inherently combinatorial nature. More specifically, identifying the optimal subset \mathbf{K}_M^* necessitates evaluating all feasible combinations of keyframes, rendering it computationally infeasible for sets comprising more than 15 – 20 keyframes. Therefore, in the subsequent section IV, we describe the proposed optimization approach to derive the optimal keyframe sample space from the optimal keyframe set \mathbf{K}_M^* .

IV. REDUNDANCY MINIMIZATION AND INFORMATION PRESERVATION

To address the aforementioned inherent challenges, we propose an approximation method for solving the problem outlined in Eq. (4)-(6). Our approach involves defining, identifying, and eliminating redundancy within a keyframe set, all while retaining the crucial information encoded in the descriptors' space. Designed for real-time operations, our solution employs a sliding window combinatorial optimization technique with just two optional tunable parameters that control the balance between the *information preservation* and the *redundancy minimization*. The primary objective is twofold: (a) to eliminate redundant samples that might degrade performance in place recognition tasks due to perceptual aliases [45] while simultaneously, (b) we aim to retain the essential information encoded in the descriptors such that the retrieval performance either remains the same or is improved while the memory allocation is decreased.

A. Redundancy in keyframes

Depending on the scanning frequency of the sensor kit integrated into the robotic platform or autonomous vehicle, along with its moving speed and the characteristics of the environment, keyframe samples may capture redundant information if they are too closely spaced. First, we establish a definition for redundancy within a local set of keyframes and subsequently, we propose a metric to quantify the redundancy between poses based on their corresponding descriptor.

Definition 1.1: A keyframe \mathbf{k} is deemed redundant within a keyframe set \mathbf{K} if its removal does not affect the optimal solution set $\bar{\mathbf{K}}$ nor the minimum value of the query process defined in Eq. (4) and does not create discontinuities in the map representation. This can be expressed as:

$$\underset{\bar{\mathbf{K}}}{\text{arg min}} g_o(\mathbf{K}_Q, \mathbf{K}_M) = \underset{\bar{\mathbf{K}}'}{\text{arg min}} g_o(\mathbf{K}_Q, \mathbf{K}_M \setminus \{\mathbf{k}\}) \quad (7)$$

and

$$g_o(\mathbf{K}_Q, \bar{\mathbf{K}}) = g_o(\mathbf{K}_Q, \bar{\mathbf{K}}') \quad (8)$$

$$\text{subject to } \delta_l \leq \|\mathbf{x}_i - \mathbf{x}_{i+1}\|_2 \leq \delta_u, \forall \mathbf{x} \in \mathbf{X}.$$

Remark 1.1: The preceding equation describes redundancy within a keyframe set, however, we can also introduce the notion of *soft redundancy*. In this case, although the optimal set $\bar{\mathbf{K}}$ may vary following the removal of a keyframe \mathbf{k} , the minimum value of g_o should remain close to the original. The underlying concept of *softness* is that even after removing a keyframe, there should exist another keyframe \mathbf{k}' nearby that still offers a viable candidate for the place recognition task, ensuring that the query keyframe retains a potential match as illustrated in Fig. 2. Therefore, following Eq. (7)-(8) we can formally express this as:

$$|g_o(\mathbf{K}_Q, \bar{\mathbf{K}}) - g_o(\mathbf{K}_Q, \bar{\mathbf{K}}')| \leq \varepsilon, \quad (9)$$

$$\text{where } f_o(\mathbf{k}_q, \mathbf{k}) \approx f_o(\mathbf{k}_q, \mathbf{k}') \text{ and } \|\mathbf{x} - \mathbf{x}'\|_2 \leq \delta,$$

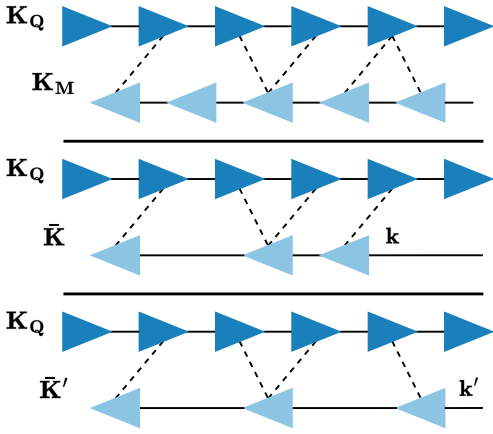


Fig. 2. **Soft redundancy.** A visual example of the map keyframes \mathbf{K}_M , the subset $\bar{\mathbf{K}} \subset \mathbf{K}_M$ that contains the corresponding nearest candidates and the same subset without the redundant keyframes. The keyframes \mathbf{k} and \mathbf{k}' both offer a match to the same query keyframe with slightly different f_σ values.

where $\delta, \varepsilon > 0$ are small positive real values, \mathbf{x}, \mathbf{x}' are the corresponding poses to the keyframe triplets \mathbf{k}, \mathbf{k}' and $\mathbf{k}_q \in \mathbf{K}_Q$ is the candidate pair for the original keyframe \mathbf{k} that, after removal, is matched with \mathbf{k}' .

Remark 1.2: The constraint specified in Eq. (8) and the concept of map discontinuity are essential to ensuring a comprehensive coverage of the map rather than achieving a continuous surface representation, given that we are dealing with 3D point clouds. More specifically, this constraint ensures the presence of a candidate keyframe across the entirety of the map. The lower and upper distance between poses, δ_l and δ_u respectively, typically ranges between 1 – 5 meters in outdoor urban environments [41], [46].

We proceed by proposing a measure that quantifies the redundancy within a keyframe set.

Definition 1.2: Given a similarity function f_σ (as previously discussed in III), the *redundancy* term ρ_τ measures the redundancy in a keyframe set \mathbf{K} and is expressed as the average similarity score between consecutive keyframe descriptors, denoted as:

$$\rho_\tau(\mathbf{K}) = \frac{1}{N-1} \sum_{i=1}^{N-1} f_\sigma(\mathbf{k}_i, \mathbf{k}_{i+1}), \quad \mathbf{k}_i \in \mathbf{K}, \quad (10)$$

where $0 < \rho_\tau(\mathbf{K}) \leq 1$ and N denotes the cardinality of the keyframe set \mathbf{K} . Higher redundancy scores, indicate high similarity between consecutive descriptors, while lower values indicate lower correlation between the keyframes.

B. Information Preservation in keyframes

In Section II, we defined the function $F: \mathbb{R}^3 \rightarrow \mathbb{R}^M$ which maps each keyframe from 3D space to an M -dimensional descriptor, thereby capturing the salient features of an environment. This function was introduced as a mapping of each observation \mathbf{z}_t , but intuitively, we recognize that $\mathbf{z}_t \propto h(\mathbf{x}_t)$, indicating that every observation is dependent

on the viewpoint, and thus the pose \mathbf{x}_t . Consequently, we can analyze the sensitivity of these descriptors to changes in pose by computing the Jacobian \mathbf{J} of F with respect to the poses \mathbf{x} , as follows:

$$\mathbf{J}_F = \begin{bmatrix} \frac{\partial \mathbf{F}}{\partial \mathbf{x}_1} & \cdots & \frac{\partial \mathbf{F}}{\partial \mathbf{x}_n} \end{bmatrix} = \begin{bmatrix} \frac{\partial F_1}{\partial \mathbf{x}_1} & \cdots & \frac{\partial F_1}{\partial \mathbf{x}_n} \\ \vdots & \ddots & \vdots \\ \frac{\partial F_m}{\partial \mathbf{x}_1} & \cdots & \frac{\partial F_m}{\partial \mathbf{x}_n} \end{bmatrix}. \quad (11)$$

To leverage this Jacobian for analyzing the function's behavior, we propose the following conjectures, grounded in the context of place recognition, where the goal is to extract consistent features from similar spatial locations.

Conjecture 2.1: For small variations in pose, the descriptor function F exhibits continuity and smoothness. Therefore, we conjecture that F is differentiable for small pose-to-pose changes. In particular, this assumption applies to both hand-crafted and learned descriptors.

Hand-crafted descriptors are typically designed to be invariant to transformations such as rotation and translation, ensuring that small pose variations induce minimal changes in the descriptor. Notable examples include Point Feature Histograms (PFH) [47], Signature of Histograms of Orientations (SHOT) [48], and Scan Context [44]. These descriptors are crafted to robustly capture distinct characteristics of the environment, but the design process requires domain expertise and extensive experimentation to guarantee both robustness and discriminative power.

Conjecture 2.2: Neural networks, when used to model the descriptor function F , are differentiable by construction, a property that is critical for gradient-based optimization algorithms such as back-propagation [49]. The differentiability of neural networks facilitates the learning of robust descriptors directly from data, complementing the use of hand-crafted features in place recognition.

Neural networks are composed of layers, each performing simple, differentiable operations. For example, a fully connected layer can be represented as $z = Wx + b$, where $x \in \mathbb{R}^n$ is the input, $W \in \mathbb{R}^{m \times n}$ is the weight matrix, $b \in \mathbb{R}^m$ is the bias term, and $z \in \mathbb{R}^m$ is the output. The output z is then passed through a non-linear activation function $a = \phi(z)$. Neural networks can also employ specialized layers, such as convolutional layers, which are commonly used in image processing. A convolutional layer applies filters to input data to capture spatial features. The output of such a layer can be expressed as:

$$z_{i,j,k} = \sum_{m,n} W_{k,m,n} x_{i+m,j+n} + b_k, \quad (12)$$

where x is the input, W are the convolutional filters, b is the bias, and z is the resulting feature map. Another prominent example is the transformer architecture, widely used in natural language processing, which utilizes a self-attention

mechanism to capture long-range dependencies in the input sequence. The self-attention mechanism is formalized as:

$$\text{Attention}(Q, K, V) = \text{softmax}\left(\frac{QK^\top}{\sqrt{d_k}}\right)V, \quad (13)$$

where Q, K, V are the query, key, and value matrices, respectively, and d_k is the dimensionality of the keys. Common activation functions ϕ include the Rectified Linear Unit (ReLU), $\phi(z) = \max(0, z)$, and the sigmoid function, $\phi(z) = 1/(1+e^{-z})$. Although ReLU is non-differentiable at $z = 0$, in practice, this singular point is typically disregarded, and when necessary, the derivative is set to zero. Given the differentiability of these components, the overall neural network function F formed by stacking layers is differentiable. Formally, for a network composed of L layers, the output y is expressed as:

$$y = F(x) = (\phi_L \circ \phi_{L-1} \circ \dots \circ \phi_1)(x). \quad (14)$$

The gradient of the output y with respect to the input x is given by:

$$\nabla_x F(x) = \frac{\partial F}{\partial x} = \frac{\partial \phi_L}{\partial \phi_{L-1}} \cdot \frac{\partial \phi_{L-1}}{\partial \phi_{L-2}} \cdot \dots \cdot \frac{\partial \phi_1}{\partial x}. \quad (15)$$

The backpropagation algorithm exploits this differentiability to efficiently compute the gradients of a loss function \mathcal{L} with respect to the network’s parameters. Specifically, for any parameter θ , the gradient is computed as:

$$\frac{\partial \mathcal{L}}{\partial \theta} = \frac{\partial \mathcal{L}}{\partial y} \cdot \frac{\partial y}{\partial \theta}. \quad (16)$$

This allows for gradient-based optimization methods to iteratively adjust the network parameters to minimize the loss function. Thus, the neural network implementation of F can be considered differentiable within the robot’s operational space, making it well-suited for place recognition tasks where continuity and smoothness are advantageous.

To sum up, both hand-crafted and neural network-based descriptors provide effective mechanisms for place recognition. Hand-crafted descriptors are carefully designed to ensure stability against small pose changes, while neural networks leverage their inherent differentiability to learn features directly from data.

Assumption 2.1: In the context of descriptor extraction and place recognition, deriving the Jacobian explicitly is often infeasible due to the complex nature of the functions involved, which are often deep neural networks. Consequently, we assume that the rate of change is obtained through numerical approximation using the available data, as illustrated on Fig. 3. This approach allows for practical computation despite the intricate nature of the functions.

Assumption 2.2: Considering the fact that the poses belongs to $SE(3)$, we simplify the dimensionality by using the Euclidean norm to measure the distance between poses, rather than taking the derivative with respect to each axis individually. In addition to this, to ensure that the Jacobian

and the rate of change are meaningful, it is essential to use descriptors that are yaw-invariant, such as those proposed in [41]–[44]. This yaw-invariance ensures that features can be tracked smoothly in the M -dimensional space, as we are not considering any derivatives related to changes in orientation.

Given these conjectures and assumptions, we consider the descriptors $\mathbf{d} \in \mathbb{R}^M$ as random variables and the poses $\mathbf{x} \in SE(3)$ as samples, then the product of the Jacobian \mathbf{J} and its transpose \mathbf{J}^\top gives us an estimate of the covariance matrix between the descriptors. Essentially, each element of this matrix indicates how much two descriptors covary across poses and can be defined as:

$$\mathbf{J}_F^\top \mathbf{J}_F = \left(\frac{\partial \mathbf{F}}{\partial \mathbf{x}}\right)^\top \left(\frac{\partial \mathbf{F}}{\partial \mathbf{x}}\right) = \mathbf{V} \mathbf{\Lambda} \mathbf{V}^{-1}, \quad (17)$$

where $\mathbf{\Lambda}$ is the $N \times N$ diagonal matrix with the eigenvalues, $\text{diag}(\mathbf{\Lambda}) = \{\lambda_1, \lambda_2, \dots, \lambda_N\}$ and \mathbf{V} is the $N \times N$ matrix whose columns are the eigenvectors $\mathbf{v}_1, \mathbf{v}_2, \dots, \mathbf{v}_N$ resulting from the decomposition process. These eigenvectors represent the principal directions of variation in the descriptor space, while the eigenvalues represent their magnitudes. As an additional preprocessing step before computing the information preservation term, we transform the descriptors using the eigenvectors obtained from the eigenvalue decomposition, $\mathbf{D}' = \sqrt{\mathbf{\Lambda}} \cdot \mathbf{V} \cdot \mathbf{D}$. This aligns the descriptors with the principal directions of maximum variability captured by the eigenvectors. Simultaneously, the descriptive vectors are scaled by the square root of eigenvalues. This scaling ensures that each dimension in the transformed data space captures variance proportional to the original data’s variability. An example of the Jacobian and the transformed descriptors can be seen on Fig. 3. Next, we define the information preservation term, which measures how well the poses in the dataset preserve the variability captured by the descriptive vectors.

Definition 2.1: The *information preservation* term π_τ for a keyframe set \mathbf{K} is expressed through the transformation of the descriptors \mathbf{D} to \mathbf{D}' using the principal components \mathbf{V} and the eigenvalues $\mathbf{\Lambda}$ from the decomposition of the covariance matrix $\mathbf{J}_F^\top \mathbf{J}_F|_{\mathbf{K}}$ and is computed as:

$$\pi_\tau(\mathbf{K}) = -\frac{1}{N-1} \sum_{i=1}^{N-1} f_\delta(\mathbf{d}'_i, \mathbf{d}'_{i+1}), \quad (18)$$

where $-1 \leq \pi_\tau(\mathbf{K}) < 0$, f_δ is the distance function between two descriptors and $\mathbf{d}' \in \mathbf{D}'$ are the transformed descriptors. Values of the information preservation term closer to zero indicate that the relationships and patterns captured by the descriptive vectors are well-preserved as poses change.

Remark 2.1: Each eigenvector \mathbf{v}_k denotes the directions of maximal variability in the descriptor space, occurring from changes in pose-to-pose distances. Within these eigenvectors, the components \mathbf{v}_{kj} signify the relative

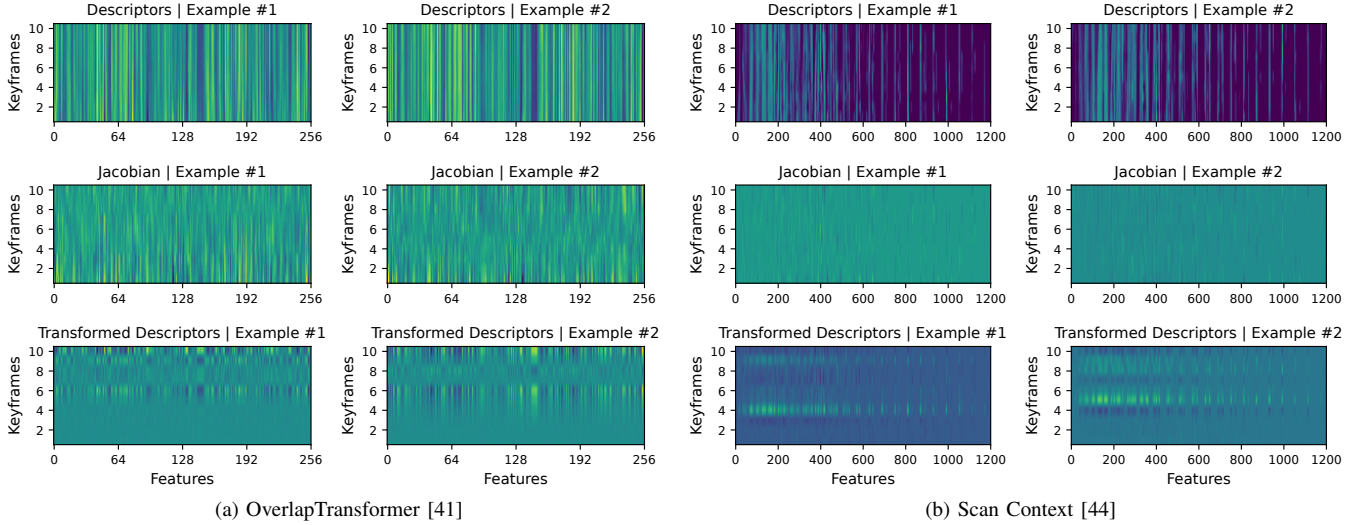


Fig. 3. **Descriptors, Jacobian and Transformed Descriptors across keyframes.** An example showing the descriptors, the Jacobian, and the transformed descriptors for two window keyframe sets. The Jacobian indicates how the features of the descriptors change between keyframes, while the transformed descriptors demonstrate how these same features appear after transformation to the principal components of that set.

contributions of each descriptor feature to the variability induced by changes in pose-to-pose distances.

Remark 2.2: The k -th eigenvalue λ_k of the covariance matrix quantifies the amount of variance described by each eigenvector \mathbf{v}_k . Larger eigenvalues indicate that the corresponding eigenvectors capture more significant patterns of variability in the data, highlighting the importance of each principal component in explaining the overall variability in the descriptor space with respect to the pose-to-pose distance.

In summary, while both ρ_τ and π_τ utilize a similarity or distance function, they differ in their objectives. The redundancy term focuses on capturing local redundancy or similarity within the keyframe set, whereas the information preservation term evaluates the conservation of information structure within the same local context, considering the variability induced by changes in pose-to-pose distances. Despite sharing similarities in computation, their distinct goals result in differing interpretations and implications for assessing the relationships between descriptive vectors within the keyframe set.

V. PROPOSED OPTIMIZATION SOLUTION

Following the definition of the two terms in the optimization function, we propose a keyframe sampling strategy tailored for LiDAR-based place recognition. Our objective is to approximate the optimal map keyframe set \mathbf{K}_M^* as defined in Section III and Eq. (5)-(6).

A. Sliding window optimization

To address the challenges posed by the computational complexity of optimizing such a large keyframe set and the non-causality of proactively selecting the best keyframes for future query sets, we introduce a sliding window optimization sampling method, summarized in Algorithm 1. By

continuously optimizing the window keyframe sets \mathbf{K}_t over the mission duration T , we accumulate them to approximate the optimal keyframe set \mathbf{K}_M^* as:

$$\mathbf{K}_M^* \cong \bigcup_{t \in [0, T]} \mathbf{K}_t^*, \quad (19)$$

where \mathbf{K}_t^* represents the minimum cardinality subset of \mathbf{K}_t that retains the maximum information. To compute the desired subset, we leverage the *redundancy* and *information preservation* terms defined earlier in Sections IV-A and IV-B respectively. The process begins with the initialization of a window keyframe set \mathbf{K}_t , containing N keyframes. The time step t progresses as soon as there are N new keyframes available, and the optimization has converged to the optimum window keyframe set \mathbf{K}_t^* . The process of finding the optimum window keyframe set is as follows: Given a window keyframe set \mathbf{K}_t , we begin by generating all possible keyframe subsets, denoted as the power set $\mathbb{P}(\mathbf{K}_t)$. The cardinality of this power set is $|\mathbb{P}(\mathbf{K}_t)| = 2^N$, providing insights into the computational complexity relative to the window size chosen. To align with the definition of the redundancy term, we impose constraints on the power set, retaining only the subsets that satisfy the constraints posed in Eq. (8), namely the minimum and maximum distance between consecutive poses. These constraints substantially reduce the size of the power set, typically by 5 – 10 times. We refer to this constrained power set as:

$$\bar{\mathbb{P}}(\mathbf{K}_t) = \{ \mathbf{K}_t^S \in \mathbb{P}(\mathbf{K}_t) : \delta_l \leq \|\mathbf{x}_i - \mathbf{x}_{i+1}\|_2 \leq \delta_u, \forall \mathbf{k} \in \mathbf{K}_t^S \}, \quad (20)$$

where \mathbf{K}_t^S represents each subset in the power set, and δ_l and δ_u denote the lower and upper distance limits for the pose-to-pose distance, typically ranging within 1 – 5 meters. We then formulate the following optimization solution, leveraging the two terms defined earlier, to search for the optimal set \mathbf{K}_t^*

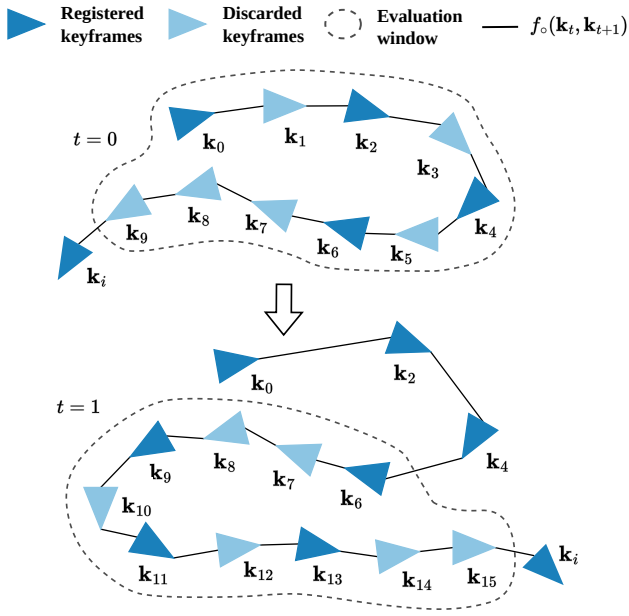


Fig. 4. **Adaptive window and keyframe re-evaluation:** An example of the adaptive window. For a window of size $N = 10$, the light blue nodes correspond to keyframes discarded by the optimization process, the last keyframe of this window is \mathbf{k}_6 . For $t = 1$, the previously discarded keyframes $\mathbf{k}_7, \mathbf{k}_8$ and \mathbf{k}_9 are part of the new evaluation window and are re-evaluated, resulting in keeping keyframe \mathbf{k}_9 that was not chosen in the previous optimization step.

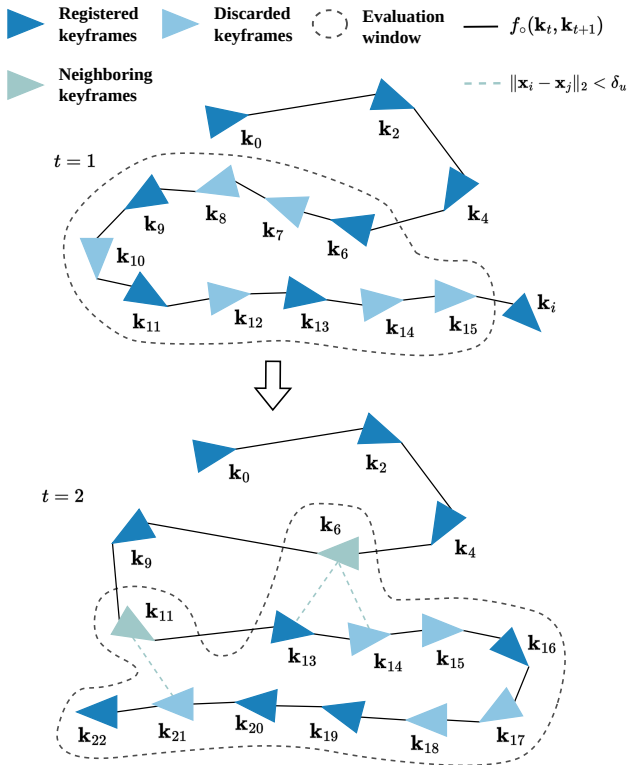


Fig. 5. **Revisiting areas:** An example of the adaptive window being extended with its neighboring keyframes. The teal nodes \mathbf{k}_6 and \mathbf{k}_{11} correspond to keyframes that are neighboring to keyframes within the optimization window and therefore are included in the evaluation process.

within the constrained power set $\bar{\mathbb{P}}(\mathbf{K}_t)$:

$$\mathbf{K}_t^* = \arg \min_{\mathbf{K}_t^S} (\rho_\tau(\mathbf{K}_t^S) + \alpha) / (\pi_\tau(\mathbf{K}_t^S) - \beta) \quad (21)$$

where $\alpha, \beta > 0$ and $\mathbf{K}_t^S \in \bar{\mathbb{P}}(\mathbf{K}_t)$.

The rationale behind this formulation is to minimize redundancy and maximize information preservation within the keyframe set. To achieve this, the minimization problem outlined above is solved through an exhaustive search. For every subset, we compute the information matrix $\mathbf{J}_F^T \mathbf{J}_F$ to capture the relationship between poses and descriptors. Subsequently, we quantify this relationship using the information preservation term from Eq. (18). Similarly, we compute the redundancy term for every subset and proceed to identify the subset with the best combined score, as per Eq. (21).

B. Adaptive window and keyframe re-evaluation

In order to provide a better approximation of the optimal keyframe set \mathbf{K}_M^* we make sure to provide a better connectivity between the optimized window keyframe sets \mathbf{K}_t^* , and thus, we define the following adaptive method for choosing the sliding interval of each window. A keyframe window, which contains N keyframes when full, is represented as:

$$\mathbf{K}_t = \{\mathbf{k}_{t,1}, \mathbf{k}_{t,2}, \dots, \mathbf{k}_{t,N}\} \quad (22)$$

After optimization, as described in Eq. (21), the optimized set is denoted as:

$$\mathbf{K}_t^* = \{\mathbf{k}_{t,i_1}, \mathbf{k}_{t,i_2}, \dots, \mathbf{k}_{t,i_n}\}, \quad (23)$$

where $1 = i_1 < i_2 < \dots < i_n \leq N$, $n < N$

and $\delta_t \leq \|\mathbf{x}_{t,i_j} - \mathbf{x}_{t,i_{j+1}}\| \leq \delta_u$

In this context, the last keyframe, \mathbf{k}_{t,i_n} , is not necessarily the last keyframe of the window prior to optimization, $\mathbf{k}_{t,N}$. For each subsequent window step $t+1$, the last chosen keyframe from the previous step becomes the first keyframe in the new step, $\mathbf{k}_{t+1,1} \leftarrow \mathbf{k}_{t,i_n}$. The remaining keyframes are inserted into the new keyframe window set as follows:

$$\begin{aligned} \mathbf{K}_{t+1} &= \{\mathbf{k}_{t+1,1}, \mathbf{k}_{t+1,2}, \dots, \mathbf{k}_{t+1,N}\} \\ &= \{\mathbf{k}_{t,i_n}, \dots, \mathbf{k}_{t,N}, \mathbf{k}_{t+1,s_t+1}, \dots, \mathbf{k}_{t+1,N}\} \end{aligned} \quad (24)$$

The number of new keyframes added in each new window step, as well as the extent of the window slide s_t , is determined adaptively based on the index of the last keyframe from the previous set:

$$s_t = N - (i_n - 1), \quad (25)$$

Thus, the new keyframe set can be rewritten with respect to the previous set as:

$$\mathbf{K}_{t+1} = \{\mathbf{k}_{t,i_n}, \dots, \mathbf{k}_{t,N}, \mathbf{k}_{t+1,N-i_n+2}, \dots, \mathbf{k}_{t+1,N}\} \quad (26)$$

This approach allows the old keyframes $\{\mathbf{k}_{t,i_n+1}, \dots, \mathbf{k}_{t,N}\}$ to be re-evaluated in the new keyframe set, as their contribution might be more significant within the new context. An example is presented in Fig. 4. Consequently, this adaptive method offers flexibility in the number of chosen keyframes

and ensures better connectivity between sliding window optimizations by avoiding fixed first and last keyframes.

C. Handling revisited areas

To effectively manage revisited areas, it is crucial to avoid redundant keyframes. At each time step t , for each keyframe window, the current optimal keyframe set \mathbf{K}_M^* is searched in conjunction with the current window keyframe set \mathbf{K}_t . The nearest neighbors are then appended to form an extended window keyframe set \mathbf{K}_t^+ , defined as:

$$\mathbf{K}_t^+ = \mathbf{K}_t \cup \{ \mathbf{k}_i : \|\mathbf{x}_i - \mathbf{x}_j\|_2 \leq \delta_u, \forall (\mathbf{x}_i, \mathbf{x}_j) \in \mathbf{K}_{M \times t}^* \}$$

where $\mathbf{K}_{M \times t}^* = \mathbf{K}_M^* \times \mathbf{K}_t$ and $\mathbf{k}_i \in \mathbf{K}_M^*$ (27)

Following the querying process, all keyframes that meet the constraint are included in the extended keyframe set, ensuring $\mathbf{K}_t^+ \supseteq \mathbf{K}_t$, as illustrated in Fig. 5. For computational efficiency, this querying process is performed using a k -NN tree, constructed from the previous optimized keyframes \mathbf{K}_M^* , resulting in the tree structure \mathcal{K}_M^* . To ensure convergence of the optimization process despite the exponential growth of search time, the set is constrained to $N + 5$ keyframes. If more than five neighbors are found, the last keyframes of \mathbf{K}_t are ignored for the current optimization cycle and automatically appended for evaluation in the next window \mathbf{K}_{t+1} . After optimizing the extended set \mathbf{K}_t^+ and acquiring \mathbf{K}_t^* , if keyframes from the neighbors are selected, they are not included in the keyframe set again. However, if these keyframes were not chosen in this optimization iteration, they are not removed from the original keyframe set. This approach ensures that neighboring keyframes are considered to evaluate the contribution of new keyframes in terms of information and redundancy, without prematurely removing past keyframes.

VI. EXPERIMENTAL SETUP AND DATASETS

The experimental setup is divided into two distinct tasks [12], as shown in Table I; *Global Place Recognition* (GPR) and *Loop Closure Detection* (LCD). The first group, GPR, involves global localization across multiple sessions, where each query frame is matched and evaluated against all map frames, as described mathematically in Eq. (4). In this task, the map keyframe set \mathbf{K}_M and the query set \mathbf{K}_Q can be from the same mapping session or different sessions taken days, weeks, or even a year apart. The second group, LCD, pertains to in-session localization, where the goal is to identify loop closure candidates for the current query frame among the nearest map frames. The primary difference here is the number of map candidates, which is significantly higher for GPR, making it more challenging. For the experimental evaluation we utilize multiple datasets, which are detailed in Subsection VI-A and briefly summarized in Table I, along with their relevant statistics, including the average and maximum speed of the vehicles, the average and maximum frame-to-frame distance and the total frames and distance of each sequence. In addition, both hand-crafted and learning-based descriptor extraction

Algorithm 1: Sliding Window Optimization

Input: 3D LiDAR scan \mathbf{z}_i , pose \mathbf{x}_i , descriptor \mathbf{d}_i
Output: Optimized keyframe set \mathbf{K}_M^*
Parameters: α, β and N

```

1 /* (default params:  $\alpha = 1, \beta = 1$  and  $N = 10$ ) */
2 /* Keyframe structure */
3 dataclass Keyframe:
4     pose: array //  $\mathbf{x} = [x, y, z, q_x, q_y, q_z, q_w]$ 
5     scan: ndarray //  $\mathbf{z} = [[x_1, y_1, z_1], \dots]$ 
6     descriptor: array //  $\mathbf{d} = [d_1, d_2, \dots, d_M]$ 
7     return k
8 /* Calculate Redundancy in a keyframe set */
9 function getRedundancy( $\mathbf{K}$ ):
10     for  $\mathbf{k}_i$  in  $\mathbf{K}$  do
11          $\rho_\tau = \rho_\tau + (1 / (1 + \|\mathbf{d}_i - \mathbf{d}_{i+1}\|))$ 
12     return  $\rho_\tau / |\mathbf{K}|$  // normalize
13 /* Calculate Information Preservation */
14 function getPreservation( $\mathbf{K}$ ):
15      $\mathbf{x} \leftarrow \|\mathbf{X}\|_2$  // pose to pose norm
16      $\mathbf{J} \leftarrow \text{gradient}(\mathbf{D}, \mathbf{x})$  // calculate Jacobian
17      $\Lambda, \mathbf{V} \leftarrow \text{eig}(\mathbf{J}^T \mathbf{J})$  // eigen decomposition
18      $\mathbf{D}' \leftarrow \sqrt{\Lambda} \cdot \mathbf{V} \cdot \mathbf{D}$  // transform descriptors
19     for  $\mathbf{d}_i$  in  $\mathbf{D}'$  do
20          $\pi_\tau = \pi_\tau + \|\mathbf{d}'_i - \mathbf{d}'_{i+1}\|_M$ 
21     return  $-\pi_\tau / |\mathbf{K}|$  // normalize
22 /* Main loop */
23 while robot is alive do
24     /* Read data and construct keyframe */
25      $\mathbf{k}_i \leftarrow \text{Keyframe}(\mathbf{x}_i, \mathbf{z}_i, \mathbf{d}_i)$ 
26     /* Add keyframes until window is full */
27     if  $|\mathbf{K}_t| < N$  then
28         append  $\mathbf{k}_i$  to  $\mathbf{K}_t$ 
29         /* Build  $k$ -NN tree */
30          $\mathcal{K}_M^* \leftarrow \text{tree}(\mathbf{K}_M^*)$ 
31         /* Check for neighbors */
32         if neighbors of  $\mathbf{k}_i$  in  $\mathcal{K}_M^*$  then
33             append neighbors to  $\mathbf{K}_t^+$ 
34     /* When the window set is full */
35     else
36         /* generate power set */
37          $\mathbb{P}(\mathbf{K}_t^+) \leftarrow \text{combinations}(\mathbf{K}_t^+)$ 
38         /* Evaluate each subset */
39         for  $\mathbf{K}_t^S$  in  $\mathbb{P}(\mathbf{K}_t^+)$  do
40              $\rho_\tau \leftarrow \text{getRedundancy}(\mathbf{K}_t^S)$ 
41              $\pi_\tau \leftarrow \text{getPreservation}(\mathbf{K}_t^S)$ 
42              $J_t \leftarrow (\rho_\tau + \alpha) / (\pi_\tau - \beta)$ 
43          $\mathbf{K}_t^* \leftarrow \arg \min J_t$ 
44         /* Update optimal keyframe set */
45         for  $\mathbf{k}_j$  in  $\mathbf{K}_t^*$  do
46             /* Only unique keyframes */
47             if  $\mathbf{k}_j$  not in  $\mathbf{K}_M^*$  then
48                 append  $\mathbf{k}_j$  to  $\mathbf{K}_M^*$ 
49         /* Update window for next iteration */
50          $\mathbf{K}_t \leftarrow \{\mathbf{k}_{t,i_n}, \dots, \mathbf{k}_{t,N}\}$ 
51         /* Next window optimization step */
52          $t \leftarrow t + 1$ 
53     /* Next data sample step */
54      $i \leftarrow i + 1$ 

```

frameworks are evaluated, to show the generalization ability of our method as well as that it is descriptor agnostic. The

evaluation metrics and the comparison targets are described and motivated in Subsection VI-C and VI-D respectively.

A. Datasets

As presented in Table I, we selected four publicly available datasets that cover a variety of urban environments and are widely used by the robotics and computer vision community. For GPR, we use the KITTI dataset [50], Apollo-SouthBay [51], and part of MulRan [52]. For LCD, we utilize the rest of the MulRan dataset and Ford Campus [53]. Combined, these datasets comprise over 1.4 million frames and 360 kilometers across more than 30 sessions. A brief description of each dataset is provided below:

1) *KITTI*: The KITTI Odometry dataset [50] is one of the most well-known and widely used datasets for benchmarking feature extraction frameworks, particularly for place recognition and loop closure detection. This dataset provides 3D LiDAR scans from the Velodyne HDL-64E sensor and ground truth poses from a GPS/IMU localization unit with RTK corrections, ensuring high accuracy in localization. For our experiments in GPR, we specifically utilize sequences 00, 02, 05, 06, 07, and 08, which include multiple revisits to the same areas. Each sequence is divided into two sessions: one for mapping and one for querying. The KITTI dataset vehicle maintains an average speed of approximately 22 to 39

km/h, depending on the sequence, with a sampling interval ranging from 0.7 to 1.1 meters.

2) *Apollo-SouthBay*: The Apollo-SouthBay dataset [51] is dedicated to place recognition tasks and encompasses several multi-session sequences across the southern San Francisco Bay Area. The dataset includes diverse urban environments and challenging scenarios to evaluate localization algorithms effectively. The San Jose sequence is structured into a mapping session and two distinct test sessions: San Jose 01 and San Jose 02, recorded more than a week apart. The ColumbiaPark sequences consist of four consecutive mapping sessions, merged into a single session, followed by a test session taken more than a month later. Finally, the Sunnyvale sequence presents a complex mapping scenario. It includes multiple sessions across different areas such as Bordeaux, Borrgas, Caspian and Geneva, Crossman, Java, Mathilda Carribean, and Mathilda Moffet, collected within a two-week period. The test session in this sequence evaluates the ability of algorithms to recognize places after a substantial time-lapse of one year, providing insights into long-term localization challenges. The dataset features 3D LiDAR scans captured using the Velodyne HDL-64E sensor and precise ground truth poses derived from a high-end GNSS RTK/INS navigation system. These attributes ensure accurate spatial and temporal

TABLE I
DATASET STATISTICS

Task	Dataset	Sequence	Avg./Max. Speed [km/h]	Avg./Max. Frame-to-frame Distance [m]	Frames		Distance [km]	
					Mapping	Querying	Mapping	Querying
Global Place Recognition (Multi-session place recognition)	KITTI [50]	Seq. 00	28.5 / 46.5	0.82 / 1.34	2,841	1,700	2.46	1.26
		Seq. 02	37.8 / 53.1	1.09 / 1.54	4,100	561	4.36	0.70
		Seq. 05	27.6 / 42.0	0.80 / 1.21	1,961	800	1.62	0.59
		Seq. 06	38.8 / 52.5	1.12 / 1.51	801	300	0.93	0.30
		Seq. 07	21.9 / 42.0	0.63 / 1.21	401	700	0.24	0.46
		Seq. 08	27.5 / 45.0	0.79 / 1.30	1,100	2,971	0.95	2.27
	Apollo-SouthBay [51]	San Jose	14.0 / 46.9	0.39 / 2.28	59,774	-	23.2	-
		San Jose 01	12.6 / 39.5	0.35 / 1.76	-	9,765	-	3.42
		San Jose 02	11.7 / 39.4	0.32 / 1.79	-	9,868	-	3.20
		ColumbiaPark	22.4 / 50.6	0.63 / 2.25	69,552	14,014	44.8	8.60
		Sunnyvale	30.2 / 82.0	0.87 / 4.65	128,937	41,170	108.1	37.8
	MulRan [52]	Sejong City 01	45.4 / 121.1	0.13 / 0.33	204,716	-	23.4	-
		Sejong City 02	45.1 / 110.3	0.13 / 0.31	-	206,219	-	23.6
		Sejong City 03	45.0 / 111.6	0.13 / 0.31	-	212,826	-	25.2
Loop Closure Detection (In-session place recogn.)	MulRan [52]	DCC 01	36.5 / 104.0	0.10 / 0.29	52,402		5.4	
		DCC 02	29.4 / 102.3	0.08 / 0.28	57,240		4.8	
		DCC 03	30.4 / 100.7	0.09 / 0.28	69,616		6.0	
		KAIST 01	33.6 / 102.3	0.08 / 0.28	78,672		7.5	
		KAIST 02	29.8 / 101.0	0.09 / 0.28	86,758		7.3	
		KAIST 03	32.2 / 100.2	0.09 / 0.28	83,868		7.7	
	Ford Campus [53]	Seq. 01	13.6 / 54.8	0.38 / 1.52	3,817		1.44	
		Seq. 02	23.6 / 56.6	0.66 / 2.35	6,103		4.00	

alignment necessary for evaluating place recognition algorithms effectively.

3) *MulRan*: The MulRan dataset [52] presents a diverse range of environments, including narrow urban roads surrounded by high-rise buildings, mountainous regions, cross-roads, rural landscapes, and urban areas featuring various structures like bridges, tunnels, and overpasses. This dataset is segmented into tasks focused on General Place Recognition (GPR) and Loop Closure Detection (LCD), with specific sequences allocated for each task: *Sejong City* for GPR, and DCC and KAIST for LCD. In the GPR task using *Sejong City*, the first session serves as the reference map data, while the subsequent two sessions (one normal and one reverse) function as test data for evaluating place recognition algorithms. Mapping and testing sessions are spaced two months apart. The dataset is captured using a 3D LiDAR sensor, specifically the Ouster OS1-64, which provides detailed point cloud information. Ground truth poses are derived from a Virtual Reference Station GPS positioning system, ensuring high accuracy in localization data. During data collection, the vehicle maintains an average speed of approximately 45 km/h in *Sejong City*, with maximum speeds exceeding 120 km/h. For the LCD sessions (DCC and KAIST), the average speeds range from 30 to 36 km/h, with peaks reaching up to 100 km/h. The dataset offers densely sampled data, with an average distance of 0.1 meters between consecutive samples, and peaks at 0.3 meters apart.

4) *Ford Campus*: The Ford Campus dataset [53] is focused on evaluating Loop Closure Detection (LCD) algorithms and comprises multiple trials conducted around the Ford research campus and downtown area in Dearborn, Michigan. This dataset offers diverse scenarios, including both small and large loops. Captured using an earlier version of the Velodyne HDL-64E 3D LiDAR sensor, the dataset provides detailed point cloud data, and the ground truth poses are derived from a GPS navigation system, ensuring accurate spatial alignment during data evaluation. Due to its smaller size and the availability of single sessions only, the Ford Campus dataset is specifically utilized for evaluating Loop Closure Detection. This dataset provides a valuable resource for testing algorithm robustness in detecting loop closures within urban and campus environments, although within a more limited scope compared to larger datasets like KITTI or MulRan.

B. Descriptor Extraction Frameworks

To evaluate how the sampling space impacts place recognition performance, we employ two state-of-the-art descriptor extraction frameworks that are publicly available. For the hand-crafted approach, we utilize Scan Context [54], which generates a feature vector of size $1 \times 20 \times 60$. This descriptor is designed to capture spatial relationships and scene context in 3D LiDAR scans, providing robustness in recognizing places across different environments. In contrast, for the learning-based approach, we utilize OverlapTransformer [41], which produces a feature vector of size 1×256 . OverlapTransformer leverages deep learning tech-

niques to learn discriminative features directly from the data, optimizing recognition performance based on the inherent overlapping characteristics of the input scans. We note that the original weights that are available by the authors are used, and no further training was conducted. By employing these frameworks, we can comprehensively evaluate the effect of sampling space on place recognition. The Scan Context++ descriptor, with its structured feature vector, offers insights into how well-defined spatial relationships contribute to recognition accuracy. Meanwhile, the OverlapTransformer, with its learned feature representation, provides a perspective on how deep learning can enhance recognition performance by leveraging larger feature spaces. Overall, this evaluation enables a comparative analysis between traditional hand-crafted descriptors and modern learning-based approaches, highlighting their respective strengths in different sampling environments and enhancing our understanding of effective place recognition strategies.

C. Evaluation Metrics

For the evaluation process, we utilize several key metrics: (i) Area Under the Precision-Recall Curve, (ii) F1-max Score and (iii) the percentage of allocated memory. Each metric is selected to provide comprehensive insights into the performance of each sampling method across different datasets and scenarios.

1) *Precision-Recall Curve*: The first metric we employ is the Area Under the Curve (AUC) of the precision-recall curve, which is particularly valuable for evaluating algorithms in scenarios with imbalanced classes, such as place recognition where revisits are infrequent. The precision-recall curve illustrates the tradeoff between precision and recall across various decision thresholds. A high AUC indicates that the algorithm achieves both high precision (low false positive rate) and high recall (low false negative rate), indicating accurate and comprehensive retrieval of positive instances. Precision is defined as the ratio of true positives to the sum of true positives and false positives, emphasizing the accuracy of positive predictions. Recall, on the other hand, measures the ratio of true positives to the sum of true positives and false negatives, highlighting the algorithm’s ability to identify all positive instances in the dataset. In summary, the AUC of the precision-recall curve provides a robust assessment of an algorithm’s performance in place recognition tasks, offering insights into its ability to effectively retrieve relevant instances while minimizing false positives and false negatives. This metric is crucial for evaluating the reliability and accuracy of place recognition systems across diverse datasets and operational conditions.

2) *F1-max Score*: The second metric we employ is the F1-max score, which combines precision and recall using their harmonic mean. This score provides a single metric that balances both precision and recall, aiming to maximize the overall performance of the algorithm. The F1 score is computed as:

$$F_1 = 2 \times \frac{\text{Precision} \times \text{Recall}}{\text{Precision} + \text{Recall}} \quad (28)$$

It ranges from 0 to 1, where 1 indicates perfect precision and recall, while 0 indicates poor performance in either metric. Maximizing the F1 score signifies achieving an optimal balance between precision (accuracy of positive predictions) and recall (ability to capture all positive instances), ensuring robustness and effectiveness in place recognition tasks. In summary, the F1-max score serves as a comprehensive metric for evaluating the overall performance of place recognition algorithms. It provides a unified measure that considers both precision and recall equally, essential for assessing an algorithm’s efficacy.

3) *Memory Allocation*: To assess the efficiency of our methods in minimizing the number of keyframes, we evaluate the memory allocation for each approach. The allocated memory percentage indicates the proportion of total memory required compared to retaining all keyframes. This metric is crucial as it measures the algorithm’s ability to reduce memory usage while maintaining effective place recognition performance. Lower percentages indicate more efficient use of memory, which is critical for real-time applications and systems with limited computational resources. By evaluating memory allocation, we ensure that our method is not only effective in reducing keyframes, but also practical and scalable for deployment in autonomous systems and robotic tasks.

D. Comparison Targets

In our comparative analysis, we evaluate various keyframe sampling methods, including three constant sampling intervals (at 1 meter, 3 meters, and 5 meters) [20]–[22], adaptive intervals based on spaciouness [32], [33], and LiDAR scan entropy [34]. These methods are compared against a baseline that uses all samples from the datasets, providing a comprehensive assessment of our proposed keyframe sampling approach’s adaptability. For our evaluations, we set the optimization parameters as: $\alpha = 1$, $\beta = 1$, and $N = 10$. These parameters govern the keyframe selection criteria, ensuring consistency and enabling direct comparisons across different methods. In subsection VII-F, we conduct an ablation study to explore how varying these parameters influences the performance of our sampling approach. Our objective is to assess how well the proposed method adapts to varying conditions and datasets compared to established sampling strategies. By examining both constant and adaptive interval methods, we aim to highlight the strengths and adaptability of our approach in optimizing keyframe selection for efficient place recognition.

VII. EXPERIMENTAL EVALUATION AND RESULTS

In this section we go through the experimental evaluation results on the aforementioned metrics as well as a detailed analysis of the optimization terms, visualizations of the sampled and clustered multidimensional descriptors using the t-distributed Stochastic Neighbor Embedding (t-SNE) [55], and visual representations of the loop closure detections. These aspects provide deeper insights into the algorithm’s behavior, highlighting its robustness and effectiveness in

diverse environments. Furthermore, we conduct an ablation study to analyze how optimization parameters impact the sampling method’s performance. This study aids in refining our approach and understanding the sensitivity of our algorithm to different settings. Lastly, we perform complexity and runtime analyses to ensure that our algorithm can operate efficiently in real-time scenarios. All these evaluations together ensure that our proposed method is not only theoretically effective but also practical for deployment in autonomous systems. By incorporating these comprehensive evaluations and analyses, we aim to validate the robustness, efficiency, and scalability of our sampling algorithm across varied datasets and operational conditions. All the experiments were realized on a 14th Gen Intel Core i9-14900K with 128GB of DDR5 RAM.

A. Does Sample Space Matter?

We begin the experimental evaluation and results section by addressing the initial question: *Does the sampling distance affect retrieval performance in place recognition?* Based on the evaluation study presented in Table II, the immediate answer is *yes*. The evaluation study presents results for the three GPR datasets and the two descriptor extraction frameworks across all sampling methods. The metrics provided include the Area Under the Precision-Recall Curve (AUC), the F1-max score, and the memory percentage allocated for storing the keyframes. Memory allocation is normalized against the baseline (All Samples), always appearing as 1.00. For ease of reading, the best method’s result from the constant intervals is underlined, while the best-performing from the adaptive methods is highlighted in bold.

Starting with the constant sampling intervals, we observe that most of the time, smaller sampling intervals result in less performance loss. There are exceptions where larger intervals improve performance beyond the baseline, such as sequence 07 from the KITTI dataset, where a 5-meter interval increases performance for OverlapTransformer, or sequence 05, where a 3-meter interval results in the least performance loss. Similarly, for Scan Context, different sessions on the KITTI dataset benefit from different constant sampling intervals, with 3 meters performing better on sequence 01 and 5 meters performing better on sequences 05 and 06.

For the other datasets, Apollo-SouthBay and MulRan, performance for both descriptors consistently decreases across all sequences. This could be attributed to the higher fidelity in frames per meter, as the KITTI dataset has a greater average frame-to-frame distance (0.85 for KITTI) compared to the others (0.50 for Apollo-SouthBay and 0.13 for MulRan). Consequently, higher sampling intervals skip fewer frames, leading to more unpredictable behavior, while datasets with higher density sampling see increased skipped frames with higher sampling distances, resulting in performance loss.

B. Retrieval Performance and Memory Allocation

We continue the discussion of the results with a quantitative and qualitative analysis. Since Table II is difficult to

compare at a glance, we present Fig. 6, which shows the precision-recall curves for all methods and GPR datasets for OverlapTransformer, and Fig. 7, which presents the deviations from the baseline for all methods in all GPR datasets for both OverlapTransformer and Scan Context.

1) *Quantitative Analysis*: Our proposed method for keyframe sampling consistently outperforms other methods in most scenarios, as depicted in Table II and Fig. 6. In contrast, the fixed interval sampling methods struggle because different sequences favor different intervals, as previously discussed.

Among the adaptive methods, the spaciousness and entropy-based approaches show varying performance depending on the dataset and sequence. The spaciousness

method, for example, rarely excels, with the KITTI 02 sequence being an exception. A significant drawback of this method is the complexity introduced by its six tunable parameters: three for defining openness thresholds and three for defining sampling intervals, making it hard to tune without any knowledge of the environment and the sensitivity of the descriptors.

The entropy-based method, while not the best performer, closely follows in many scenarios, such as the Apollo-SouthBay Sunnyvale sequence and the MulRan Sejong City 02 session. This method relies on a single parameter, the information gain threshold, that triggers keyframe sampling. Its effectiveness comes from directly comparing consecutive point cloud scans to assess the new information

TABLE II

QUANTITATIVE RESULTS FOR THE PERFORMANCE OF ALL EVALUATED METHODS USING OVERLAPTRANSFORMER (OT) AND SCAN CONTEXT (SC).

Dataset	Sequence	Metric	All Samples		Constant at 1m		Constant at 3m		Constant at 5m		Spaciousness		Entropy-based		Optimized (Ours)	
			OT	SC	OT	SC	OT	SC	OT	SC	OT	SC	OT	SC	OT	SC
KITTI Odometry	Seq. 00	F1-MAX	0.96	0.83	<u>0.95</u>	0.80	0.94	<u>0.81</u>	0.85	0.79	0.92	0.80	0.90	0.80	0.94	0.80
		AUC	0.99	0.87	<u>0.99</u>	0.82	0.98	<u>0.84</u>	0.94	0.84	0.98	0.81	0.97	0.81	0.99	0.83
		MEM.	1.00		0.66		0.25		0.16		0.36		0.33		0.54	0.33
	Seq. 02	F1-MAX	0.78	0.75	<u>0.79</u>	<u>0.62</u>	0.75	0.52	0.68	0.47	0.82	0.90	0.66	0.67	0.76	0.86
		AUC	0.82	0.76	<u>0.83</u>	<u>0.59</u>	0.72	0.54	0.65	0.42	0.85	0.89	0.67	0.64	0.82	0.95
		MEM.	1.00		0.82		0.30		0.19		0.40		0.31		0.68	0.61
	Seq. 05	F1-MAX	0.91	0.94	0.91	0.53	<u>0.91</u>	0.80	0.86	<u>0.83</u>	0.91	0.79	0.86	0.79	0.91	0.75
		AUC	0.98	0.95	0.97	0.57	<u>0.97</u>	0.84	0.93	<u>0.91</u>	0.97	0.84	0.93	0.86	0.97	0.82
		MEM.	1.00		0.65		0.24		0.15		0.28		0.30		0.54	0.50
	Seq. 06	F1-MAX	0.96	0.87	<u>0.96</u>	0.95	0.94	0.95	0.89	<u>0.97</u>	0.92	0.96	0.91	0.90	0.95	0.97
		AUC	0.99	0.92	<u>0.99</u>	0.98	0.97	0.99	0.94	<u>0.99</u>	0.95	0.99	0.95	0.96	0.98	0.99
		MEM.	1.00		0.85		0.30		0.21		0.26		0.34		0.69	0.72
	Seq. 07	F1-MAX	0.67	0.92	0.64	<u>0.89</u>	0.69	0.87	<u>0.76</u>	0.87	0.65	0.87	0.66	0.89	0.67	0.90
		AUC	0.77	0.94	0.73	<u>0.96</u>	0.75	0.94	<u>0.82</u>	0.92	0.72	0.93	0.74	0.94	0.77	0.96
		MEM.	1.00		0.51		0.19		0.12		0.24		0.26		0.41	0.39
	Seq. 08	F1-MAX	0.29	0.75	<u>0.30</u>	<u>0.57</u>	0.28	0.46	0.24	0.53	0.26	0.50	0.28	0.52	0.32	0.72
		AUC	0.22	0.80	<u>0.18</u>	<u>0.63</u>	0.16	0.53	0.14	0.58	0.14	0.55	0.20	0.59	0.20	0.81
		MEM.	1.00		0.62		0.25		0.16		0.27		0.28		0.52	0.45
Apollo-SouthBay	SanJose01	F1-MAX	0.86	0.98	<u>0.86</u>	<u>0.97</u>	0.80	0.92	0.59	0.89	0.85	0.88	0.57	0.95	0.86	0.97
		AUC	0.89	0.99	<u>0.89</u>	<u>0.99</u>	0.79	0.97	0.51	0.93	0.87	0.93	0.44	0.98	0.88	0.99
		MEM.	1.00		0.28		0.12		0.08		0.10		0.20		0.47	0.33
	SanJose02	F1-MAX	0.95	0.94	<u>0.94</u>	<u>0.94</u>	0.75	0.90	0.56	0.81	0.56	0.82	0.88	0.92	0.95	0.94
		AUC	0.91	0.99	<u>0.87</u>	0.98	0.58	0.95	0.35	0.89	0.35	0.88	0.80	0.97	0.90	0.99
		MEM.	1.00		0.28		0.12		0.08		0.08		0.20		0.48	0.32
	Columbia	F1-MAX	0.94	0.96	<u>0.93</u>	<u>0.96</u>	0.84	0.93	0.68	0.90	0.68	0.91	0.89	0.94	0.92	0.96
		AUC	0.89	0.99	<u>0.87</u>	<u>0.99</u>	0.75	0.98	0.52	0.97	0.52	0.97	0.80	0.98	0.84	0.99
		MEM.	1.00		0.48		0.19		0.12		0.12		0.27		0.41	0.45
	Sunnyvale	F1-MAX	0.89	0.93	<u>0.88</u>	<u>0.93</u>	0.83	0.81	0.72	0.75	0.65	0.76	0.85	0.87	0.88	0.88
		AUC	0.85	0.96	<u>0.83</u>	<u>0.95</u>	0.75	0.86	0.60	0.81	0.50	0.82	0.79	0.90	0.82	0.93
		MEM.	1.00		0.40		0.23		0.15		0.17		0.23		0.43	0.36
MulRan	Sejong 02	F1-MAX	0.62	0.85	<u>0.58</u>	<u>0.85</u>	0.47	0.84	0.44	0.80	0.48	0.83	0.55	0.84	0.56	0.85
		AUC	0.54	0.82	<u>0.51</u>	<u>0.82</u>	0.40	0.81	0.35	0.77	0.42	0.81	0.46	0.81	0.49	0.82
		MEM.	1.00		0.60		0.22		0.15		0.22		0.50		0.52	0.55
	Sejong 03	F1-MAX	0.55	0.57	<u>0.54</u>	<u>0.57</u>	0.35	0.30	0.31	0.22	0.38	0.32	0.44	0.45	0.55	0.55
		AUC	0.45	0.46	<u>0.44</u>	<u>0.46</u>	0.23	0.22	0.18	0.15	0.42	0.26	0.30	0.34	0.43	0.45
		MEM.	1.00		0.60		0.22		0.15		0.22		0.51		0.52	0.55

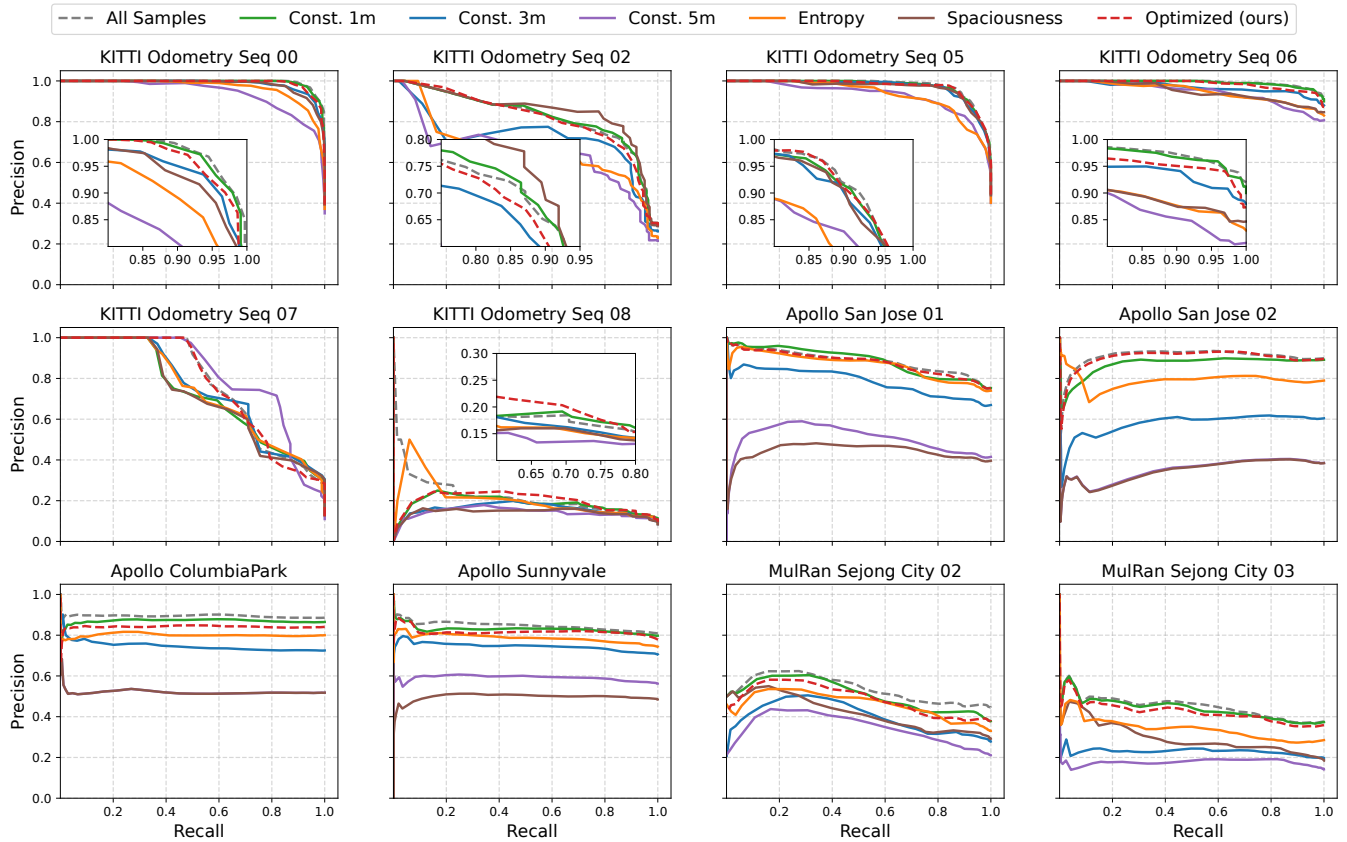


Fig. 6. **Precision-recall curves.** Results for *Global Place Recognition* in KITTI, Apollo-SouthBay and MulRan, using the OverlapTransformer descriptors.

and features available. Although it is not directly connected to the feature space used in place recognition, it still provides a better solution than the spaciousness method, which only measures how open/closed a space is.

Our proposed methodology proves superior by outperforming all other methods for both descriptor extraction frameworks across most evaluated sequences. The direct optimization of the keyframe sampling process in the descriptor feature space provides a significant advantage that boosts performance. The trade-off of a minor performance loss compared to lower memory allocation percentages is justifiable for long-term robotic missions.

2) *Qualitative Analysis:* For the qualitative analysis, we conducted a statistical examination of the results presented in Table II. Figure 7 illustrates the deviations from the baseline performance (All Samples) for both the AUC and F1-max metrics, as well as memory allocation, expressed as a percentage of overall performance gain or loss. The top sub-figure in Fig. 7 displays results for the OverlapTransformer descriptors, while the bottom sub-figure shows the results for the Scan Context descriptors. The constant 1-meter interval maintains good performance with minimal deviations around zero. However, as the sampling distance increases, performance drops significantly for OverlapTransformer, while Scan Context experiences a less drastic decline. Notably, the large min/max values for memory usage with the constant 1-meter interval result from different sampling resolutions in the datasets. For instance, the KITTI dataset, with an average

frame-to-frame distance of 0.85 meters, results in higher memory usage since a 1-meter interval retains almost all samples. In contrast, datasets like MulRan, with an average frame-to-frame distance of 0.13 meters, see memory usage reductions down to 30%.

Examining the adaptive methods, the spaciousness ap-

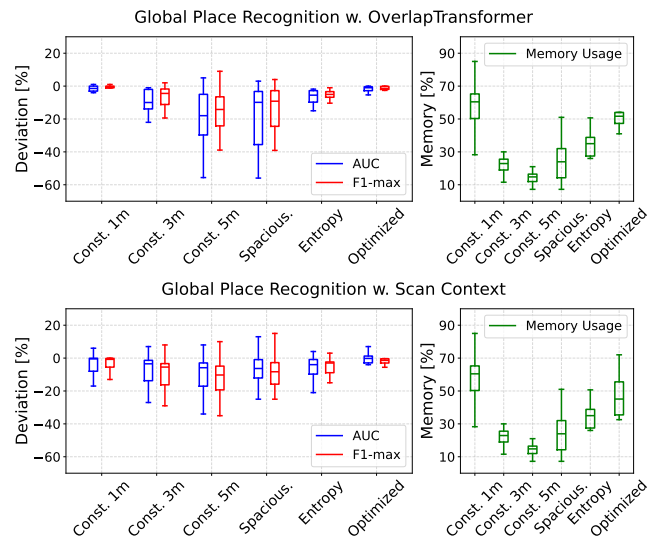


Fig. 7. **Performance deviations.** Box plots for the deviation from the baseline (All Samples) for all methods evaluated on the GPR datasets. The top figure corresponds to results using the OverlapTransformer descriptors, while the bottom figure refers to the results using the Scan Context descriptors.

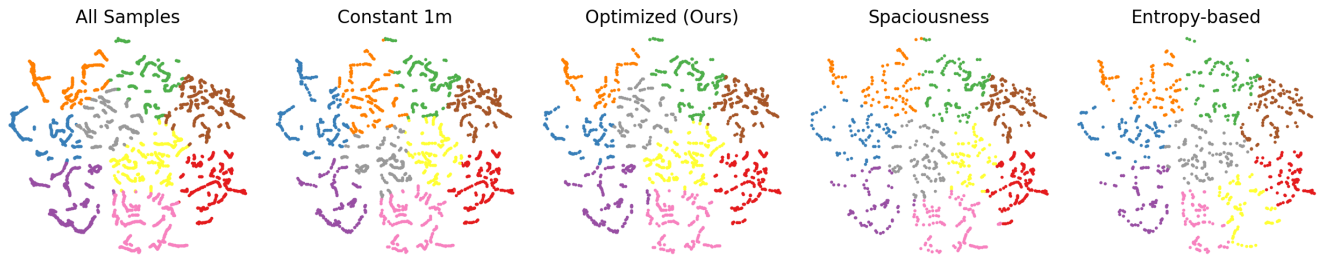


Fig. 8. **t-SNE visualization.** The clustered descriptors after the dimensionality reduction for each sampling method. Results are shown for the KITTI 00 sequence using the OverlapTransformer descriptors.

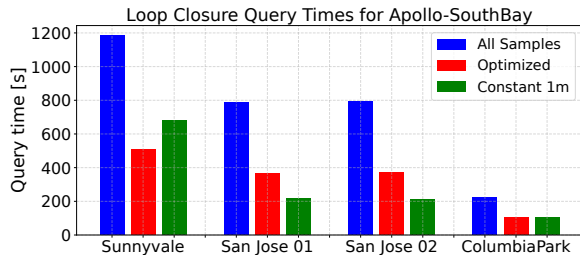


Fig. 9. **Loop Closure Detection query times.** Bar plots of the loop closure detection time between the map and query keyframes, on the Apollo-SouthBay dataset for different methods.

proach proves unstable, with significant deviations and performance losses of up to 40%, and an average performance drop of around 10% for OverlapTransformer. For Scan Context, spaciousness shows more stability, with losses up to 25% and gains up to 15%, averaging around a 10% loss for both AUC and F1-max. Conversely, the entropy-based method performs better, with less variability and an average loss of approximately 5% for both descriptors. The overall median, minimum, and maximum values demonstrate the effectiveness of our proposed approach in maintaining strong performance compared to both adaptive and fixed interval methods. The minimal spread in AUC and F1-max score indicates consistent retention of performance across both descriptor extraction frameworks. Additionally, the significant deviation in memory allocation underscores our method’s adaptability, efficiently retaining as many samples as necessary to maintain performance. In contrast, both the entropy-based and spaciousness methods fail to adapt effectively in most scenarios. These results highlight the advantages of our proposed approach, which requires no tuning and dynamically adapts to the environment. Fixed intervals offer varying benefits across different environments, and both the entropy-based and spaciousness methods require tuning and extensive knowledge of the environment to adapt, making them less efficient and more challenging to use.

3) *Loop Closure Detection Query Time:* To emphasize the importance of memory reduction and keyframe sparsification, we compare the loop closure detection query times of our optimized sampling method against the constant 1-meter interval and the baseline method that retains all samples, as shown in Fig. 9. For the Apollo-SouthBay dataset and its four sequences, we measure the time taken to query each keyframe against all map keyframes and present the results. In large-scale missions, thousands of accumulated frames can lead to significant computational times when identifying

inter- and intra-robot loop closures [23], [24]. Fig. 9 illustrates the time required to query the map descriptors with the query frames using OverlapTransformer. The results show that the baseline approach of retaining all samples results in high computational times, reaching up to 1200 seconds. In contrast, our optimized sampling method reduces query time to around 500 seconds, less than half of the baseline time.

4) *Descriptor Sensitivity:* Through this evaluation study, it is evident that each descriptor extraction framework, whether handcrafted or learning-based, is affected differently by the sampling interval. We observe that Scan Context exhibits a less drastic decrease in performance as the sampling interval increases, whereas OverlapTransformer is much more sensitive to these changes. This sensitivity could be attributed to OverlapTransformer being a trained model that was optimized on a constant threshold, thus struggling to generalize beyond its training parameters. In contrast, handcrafted descriptors are designed to extract discriminative features, and if the environment maintains consistent features over several meters, these descriptors can still effectively capture and represent them in the descriptor space. The *key takeaway* here is that when developing feature extraction frameworks with the goal of real-world deployment, it is crucial to discuss and analyze the impact of the sampling interval. Performing a sensitivity study will provide practitioners with a clear understanding of how different intervals affect performance, enabling them to deploy the frameworks more effectively. This consideration is vital for ensuring robustness and reliability in various environmental conditions and application scenarios.

C. Quantification of the optimization terms

To further validate the optimization formulation’s performance, we analyze the individual optimization terms and their effectiveness in describing each keyframe set. Table III

TABLE III
MEASURE OF REDUNDANCY AND INFORMATION PRESERVATION
ACCORDING TO THE OPTIMIZATION TERMS

Dataset	Term	All Samples	Const. at 1m	Spaciousness	Entropy-based	Optimized (Ours)
KITTI	$\rho_\tau \downarrow$	0.88	0.56	0.29	0.26	0.45
	$\pi_\tau \uparrow$	-0.14	-0.19	-0.31	-0.28	-0.20
Apollo-SouthBay	$\rho_\tau \downarrow$	0.89	0.25	0.07	0.17	0.42
	$\pi_\tau \uparrow$	-0.15	-0.17	-0.22	-0.19	-0.15
MulRan	$\rho_\tau \downarrow$	0.96	0.57	0.20	0.48	0.49
	$\pi_\tau \uparrow$	-0.05	-0.06	-0.11	-0.07	-0.06

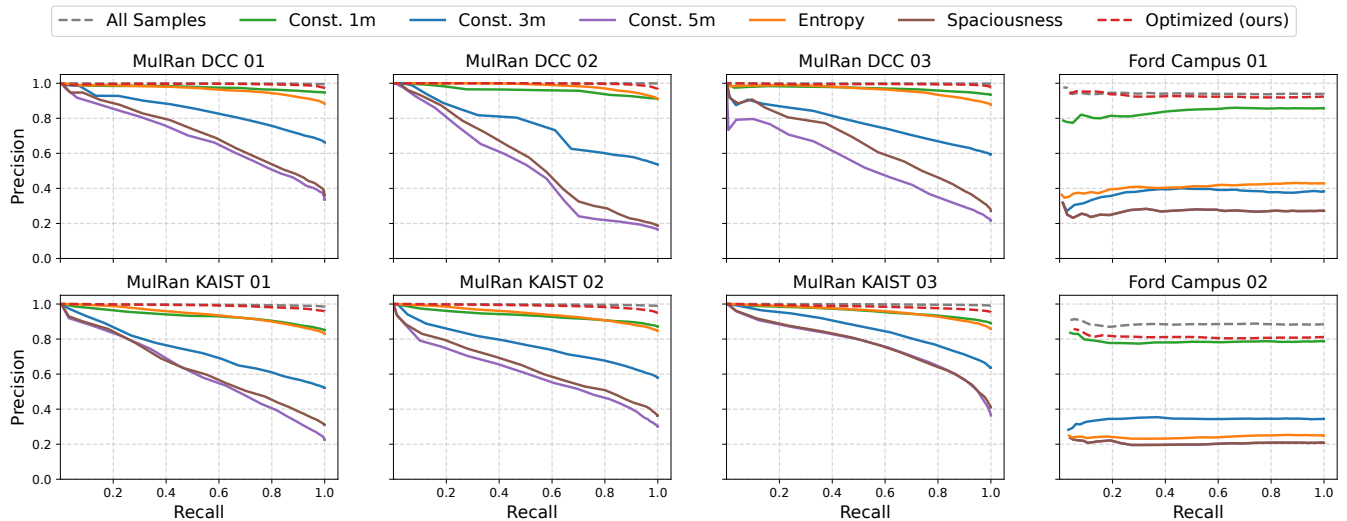


Fig. 10. **Precision-recall curves.** Loop Closure Detection in MulRan and Ford Campus datasets using the OverlapTransformer descriptors.

presents the results from the 00 sequence of KITTI, the San Jose sequence of Apollo-SouthBay, and the Sejong City sequence of MulRan. For the redundancy term ρ_τ , we compare the sampled map keyframe set from each sampling method against retaining all samples, calculated according to Eq. (10). Due to the infeasibility of decomposing large keyframe sets for the information preservation term π_τ , we calculate it, according to Eq. (10), over a sliding window of ten keyframes, averaging the results. As discussed in sections IV-A and IV-B, lower redundancy and higher information preservation (close to zero) are desirable. Table III shows that for the 00 sequence of KITTI, the 1-meter interval and the proposed optimization method perform best, while the spaciousness and entropy-based methods have low redundancy but significantly lower information preservation. This pattern is consistent across the other two sequences,

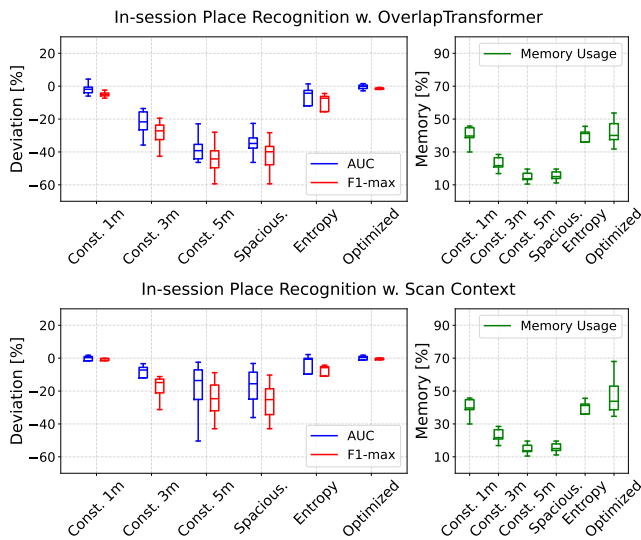


Fig. 11. **Performance deviations.** Box plots for the deviation from the baseline (All Samples) for all methods evaluated on the LCD datasets. The top figure corresponds to results using the OverlapTransformer descriptors, while the bottom figure refers to the results using the Scan Context descriptors.

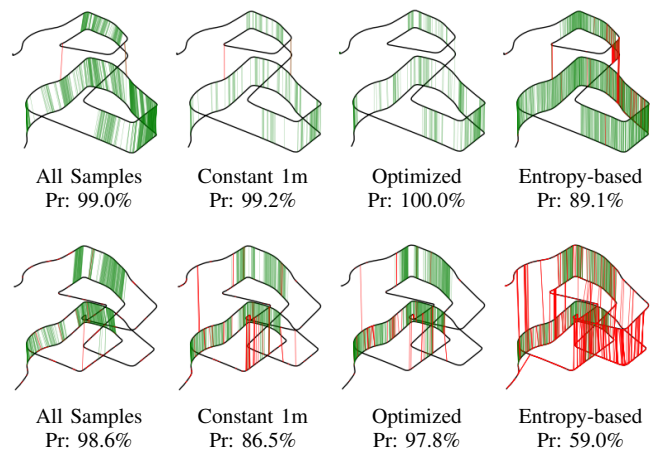


Fig. 12. **Example of loop closures detected.** Scan Context is used on the DCC 01 (top) sequence and OverlapTransformer on the DCC 03 (bottom) sequence of MulRan, for different sampling methods, along their precision.

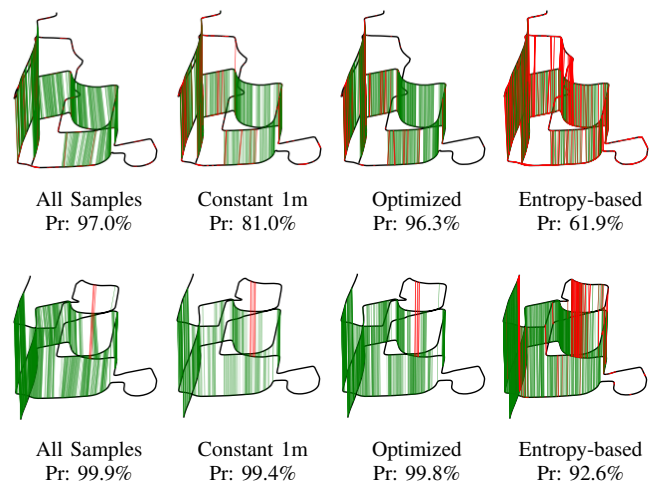


Fig. 13. **Example of loop closures detected.** OverlapTransformer is used on the KAIST 01 (top) sequence and Scan Context on the KAIST 02 (bottom) sequence of MulRan, for different sampling methods, along their precision.

where the optimized method balances reduced redundancy and increased information preservation compared to the baseline, and these results validate the performance previously demonstrated in Fig. 6.

D. Visualizing the clusters with *t*-SNE

We further analyze the impact of the sampling methods on the ability of a keyframe set to represent a dataset in the hyper-dimensional space. To achieve this, we first apply the *t*-SNE dimensionality reduction algorithm to the full set of descriptors, allowing for visualization in two dimensions. Then, for each method, we cluster the sampled keyframes based on their reduced-dimension descriptors. Fig. 8 illustrates the *t*-SNE plots for the KITTI 00 sequence, comparing the baseline (All Samples) with the 1m constant interval and the three adaptive methods, including our proposed optimized method. The different colors represent the distinct clusters. Upon examining Fig. 8, it is evident that only our optimized sampling method preserves the clustering patterns seen in the baseline. While the 1-meter interval maintained a higher number of keyframes it still alters the clustering, similarly to the spaciousness and entropy-based methods that result in significant deviations. This analysis highlights that our optimization approach effectively discards keyframes while maintaining the original hyper-dimensional structure of the keyframe set.

E. Real-time loop closure detection evaluation

Continuing our evaluation, we now turn to the LCD datasets as outlined in Table I. The results presented in Fig. 10, 11, 12 and 13 correspond to loop closure detection using the 25 nearest neighbors from the accumulated map keyframes with *k*-NN, applying a 5-meter threshold to classify candidates as hits or misses. Figure 10 shows the precision-recall curves for all methods and datasets using the OverlapTransformer descriptors, while Fig. 11 illustrates deviations from the baseline for all methods with both OverlapTransformer and Scan Context descriptors. As with the GPR datasets, the proposed optimization sampling method consistently outperforms the other adaptive methods, while also demonstrating an advantage over the 1-meter interval approach. As discussed in Section VI-A, the LCD task is generally less challenging since the best candidate search is confined to nearby candidates, reducing the likelihood of false positives. Consequently, the entropy-based approach performs significantly better in this task compared to the GPR results, as the entropy threshold samples consecutive keyframes, offering a more localized separation rather than a global one. Interestingly, the constant 1-meter sampling method exhibits a performance drop on the Ford Campus dataset. This decline could be attributed to the dataset’s larger average resolution between poses, 0.38 and 0.66 meters, respectively, for the two sequences, as shown in Table I. When map keyframes are sampled more sparsely, the 25 nearest candidates cover a wider area of the map, increasing the risk of perceptual aliasing while also potentially excluding the best match from the sampled keyframes. This explains

the significant performance decline as the constant sampling interval increases to 3–5 meters.

The deviations from the baseline illustrated in Fig. 11 indicate that the proposed optimized approach maintains stable performance with minimal losses while reducing memory overhead by 50-60%. Similar to the GPR results shown in Fig. 7, the OverlapTransformer and Scan Context descriptors exhibit different levels of sensitivity across the various sampling methods, with OverlapTransformer being particularly more sensitive. Finally, Fig. 12 and Fig. 13 provide examples from different sessions within the MulRan dataset, showcasing the expected outcomes of the LCD task for both descriptor extraction frameworks. More specifically, Fig. 12 presents the DCC 01 and DCC 02 sequences for Scan Context and OverlapTransformer, respectively, while Fig. 13 illustrates the KAIST 02 and KAIST 03 sequences for OverlapTransformer and Scan Context, respectively. The trajectory of each sequence is plotted with *x* and *y* coordinates, with time represented on the *z*-axis. For each sampling method, the precision percentage is provided, highlighting the superior performance of the optimized method, which closely aligns with the baseline performance of using all samples.

F. Ablation Study and Computational Complexity

Additionally, we conducted an ablation study on the KITTI dataset in order to investigate the individual contributions of the two optimization terms, ρ_τ and π_τ , as well as the effects of changing the optimization parameters α and β , and the window size *N* on performance and computational complexity. The results are presented in Table IV and refer to the mean and standard deviation of the difference from the baseline (All Samples), across all KITTI sequences. Negative values indicate loss of performance compared to the baseline, while positive values indicate gain of performance.

First, focusing on optimizing each term independently, we observe distinct behaviors. Minimizing redundancy (ρ_τ) slightly reduces memory allocation but leads to larger deviations in performance, particularly in terms of the AUC. Conversely, optimizing solely for information preservation (π_τ) results in higher memory allocation with lower deviations in AUC and F1-max, indicating a more robust performance across sequences. Next, we explore the impact of tuning α and β parameters. Default tuning ($\alpha = \beta = 1$) strikes a balance between performance and memory allocation, while alternating parameters with a ratio of 4, demonstrates slight performance and memory consumption benefits respectively for each optimization term.

The window size affects computational speed as the number of keyframes increases. Despite notable changes in computational time with different window sizes (5, 10, and 15 keyframes), the performance remains relatively stable, with only minimal gains for larger window sizes. A window size of 10 keyframes strikes a balance between performance and computational time, averaging 14.4 ms for KITTI, making it suitable for real-time operations, especially since most LiDAR-Inertial Odometry (LIO) packages provide odometry

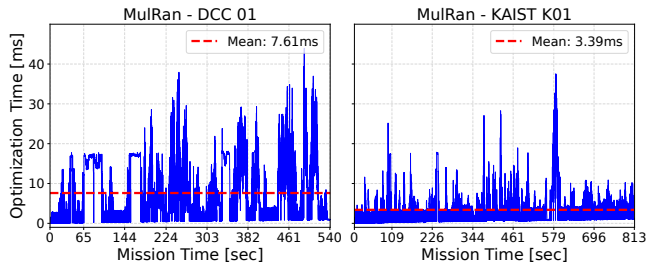


Fig. 14. **Optimization times.** Per instance optimization time across mission time, for the DCC 01 and KAIST 01 sequences of the MulRan dataset.

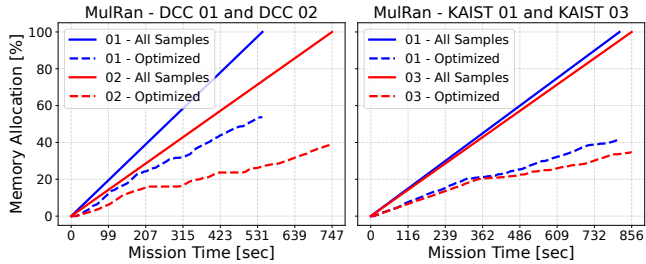


Fig. 15. **Memory allocation.** Displayed across time, for various sequences.

at 10-20 Hz. Due to constraints on pose distance, not all subset combinations are evaluated, resulting in a computational complexity of $\mathcal{O}(n \log n)$ rather than $\mathcal{O}(2^n)$. This reduction in complexity is evident in Fig. 14, where the mean optimization time for the MulRan sequences is less than that for KITTI. This discrepancy arises because MulRan has a lower average frame-to-frame distance, so fewer subsets meet the distance criteria of Eq. (20), leading to faster optimization with fewer subsets to evaluate. Finally, Fig. 15 illustrates a direct comparison of the memory allocation for the keyframes over the duration of various missions from the MulRan dataset. It is evident that the proposed

TABLE IV

RESULTS OF THE ABLATION STUDY ARE PRESENTED AS THE MEAN AND STANDARD DEVIATION DIFFERENCES FROM THE BASELINE (ALL SAMPLES) FOR THE AUC, F1-MAX SCORE, AND MEMORY, AS WELL AS THE MINIMUM/AVERAGE/MAXIMUM VALUES RESPECTIVELY FOR THE WINDOW OPTIMIZATION TIMES IN MILLISECONDS.

	Metrics	AUC [%]	F1-MAX [%]	MEM. [%]	TIME
$N = 5$	only ρ_τ	-1.74 ± 5.75	-1.27 ± 3.74	37.9 ± 12.5	$0.08 / 0.51 / 2.49$
	only π_τ	1.84 ± 3.75	0.62 ± 3.18	49.1 ± 14.1	
	$\alpha = 1, \beta = 1$	-0.43 ± 3.03	-0.84 ± 2.81	54.0 ± 6.38	
	$\alpha = 4, \beta = 1$	-0.40 ± 4.16	-0.49 ± 2.46	38.2 ± 11.3	
	$\alpha = 1, \beta = 4$	1.74 ± 3.78	0.79 ± 2.47	42.9 ± 14.3	
$N = 10$	only ρ_τ	1.02 ± 5.43	0.64 ± 3.36	42.7 ± 14.7	$0.92 / 14.4 / 32.9$
	only π_τ	1.64 ± 3.38	1.02 ± 2.50	42.0 ± 15.6	
	$\alpha = 1, \beta = 1$	1.42 ± 3.40	0.71 ± 2.36	43.8 ± 13.6	
	$\alpha = 4, \beta = 1$	1.21 ± 3.13	0.40 ± 2.32	42.0 ± 16.2	
	$\alpha = 1, \beta = 4$	1.57 ± 2.34	0.95 ± 2.40	46.2 ± 15.6	
$N = 15$	only ρ_τ	1.67 ± 5.09	0.79 ± 3.27	41.2 ± 16.3	$32 / 398 / 952$
	only π_τ	1.96 ± 3.28	1.13 ± 2.37	43.8 ± 16.3	
	$\alpha = 1, \beta = 1$	1.63 ± 3.25	0.84 ± 2.24	44.3 ± 15.7	
	$\alpha = 4, \beta = 1$	1.74 ± 3.18	1.47 ± 2.63	41.3 ± 15.5	
	$\alpha = 1, \beta = 4$	2.02 ± 3.26	1.03 ± 2.31	43.5 ± 16.1	

optimized keyframe sampling method offers a less rapid memory allocation rate and is able to maintain far less keyframes over time, providing more resources for long term and larger scale missions.

VIII. DISCUSSION

A. Note to Practitioners

A key takeaway from this study is the critical importance of sampling strategy when deploying place recognition frameworks, particularly for loop closure detection, where performance is crucial. High rates of false positives can lead to significant issues in subsequent pose graph optimization steps. We strongly advise practitioners to carefully assess their system’s memory and computational capacity in order to select additional algorithms that will ensure robust performance. Before real-world deployment, it is essential to thoroughly evaluate the chosen descriptor extraction framework to gauge its performance, adaptability, and sensitivity to sampling distance. Based on our findings, we recommend selecting a small sampling interval between poses if the system can support it, keeping in mind that this approach may not scale well for large environments. In scenarios where the environment is unknown, tuning adaptive methods based on entropy or spatial distribution can be challenging, so for a constant interval, we suggest keeping it as small as the system allows. For those interested in integrating our proposed method, it is available on our GitHub page¹. We recommend using the default parameters of $\alpha = \beta = 1$ and $N = 10$. Additionally, we provide example classes such as KITTI_Handler and OT_Handler, which include the necessary functions to apply the proposed method with any dataset and descriptor extraction framework you may wish to experiment with.

B. Limitations

The proposed approach comes with a few limitations. First, the method currently lacks mechanisms to filter out noisy LiDAR scans, which could lead to false positive descriptor matching, or to exclude samples where LiDAR data may be distorted due to rapid motion, resulting in undesired descriptors. Second, the effectiveness of the proposed optimization approach is highly dependent on the quality of the descriptors used, meaning that the choice of place recognition framework will significantly impact the performance of the sampling strategy. Therefore, we strongly recommend that practitioners thoroughly test their chosen descriptors before deploying them in real-world scenarios. Lastly, it is important to note that, as described in Section III, the problem formulation does not guarantee a globally optimal solution for the keyframe set. However, this limitation is inherent to the problem itself rather than a shortcoming of the proposed approach.

¹<https://github.com/LTU-RAI/opt-key>

C. Future Work

Future work will focus on addressing the first limitation mentioned, by incorporating motion and noise filters to ensure that the point cloud data used for descriptor extraction is valid, thereby preventing unwanted behaviors. Another direction for future research is extending the optimized sampling approach to other challenges, such as pose graph optimization. The generic nature of our solution, which optimizes the keyframe set directly in the descriptor space, could be highly beneficial for related problems, like reducing the number of keyframes in pose graph optimization, thereby enhancing efficiency and long-term viability. Additionally, we aim to extend this work to multi-agent systems, where the optimization could be distributed among multiple agents. This would reduce communication overhead and increase the overall efficiency of the system.

IX. CONCLUSIONS

In conclusion, our research has introduced a novel framework for enhancing the efficiency of global localization tasks in robotics, particularly focusing on place recognition through LiDAR-based keyframe selection. Through our investigation into the concept of sampling space and the formal mathematical formulation we introduced, we have prompted important questions within the robotics community regarding the optimization of sampling strategies for improved long term SLAM performance. Our proposed solution, which minimizes redundancy and preserves information, offers a robust approach, effectively reducing memory overhead while maintaining high retrieval performance. Unlike fixed interval solutions and other adaptive methods, our solution does not necessitate precise tuning, which can be challenging in unknown environments. The evaluation conducted across public datasets, including both learning-based and handcrafted descriptors, has underscored the efficacy and robustness of our methodology across various scenarios. These findings underscore the potential of our approach to advance global localization techniques, opening the way for more efficient and practical robotic applications in various settings. Looking ahead, future research could explore further optimizations in keyframe selection algorithms and delve deeper into the implications of sampling space in place recognition, thereby unlocking new possibilities for autonomous navigation, exploration, and beyond.

REFERENCES

- [1] G. Mehr, P. Ghorai, C. Zhang, A. Nayak, D. Patel, S. Sivashangaran, and A. Eskandarian, "X-CAR: An Experimental Vehicle Platform for Connected Autonomy Research," *IEEE Intelligent Transportation Systems Magazine*, vol. 15, pp. 41–57, 2022.
- [2] S. Nordström, N. Stathoulopoulos, N. Dahlquist, B. Lindqvist, I. Tevetzidis, C. Kanellakis, and G. Nikolakopoulos, "Safety Inspections and Gas Monitoring in Hazardous Mining Areas Shortly After Blasting Using Autonomous UAVs," *TechRxiv*, vol. 23, p. 1.
- [3] A. Agha, K. Otsu, B. Morrell, D. Fan, R. Thakker, A. Santamaria-Navarro, S.-K. Kim, A. Bouman, *et al.*, "NeBula: TEAM CoSTAR's Robotic Autonomy Solution that Won Phase II of DARPA Subterranean Challenge," *Field Robotics*, vol. 2, no. 1, pp. 1432–1506, 2022.
- [4] B. Lindqvist, A. Patel, K. Löfgren, and G. Nikolakopoulos, "A Tree-Based Next-Best-Trajectory Method for 3-D UAV Exploration," *IEEE Transactions on Robotics*, vol. 40, pp. 3496–3513, 2024.
- [5] C. Cadena, L. Carlone, H. Carrillo, Y. Latif, D. Scaramuzza, J. Neira, I. Reid, and J. J. Leonard, "Past, Present, and Future of Simultaneous Localization and Mapping: Toward the Robust-Perception Age," *IEEE Transactions on Robotics*, vol. 32, no. 6, pp. 1309–1332, 2016.
- [6] J. A. Placed, J. Strader, H. Carrillo, N. Atanasov, V. Indelman, L. Carlone, and J. A. Castellanos, "A Survey on Active Simultaneous Localization and Mapping: State of the Art and New Frontiers," *IEEE Transactions on Robotics*, vol. 39, no. 3, pp. 1686–1705, 2023.
- [7] K. Ebadi, L. Bernreiter, H. Biggie, G. Catt, Y. Chang, A. Chatterjee, C. E. Denniston, S.-P. Deschênes, K. Harlow, S. Khattak, L. Nogueira, M. Palieri, P. Petráček, M. Petrlik, A. Reinke, R. Krátký, S. Zhao, A.-a. Agha-mohammadi, K. Alexis, C. Heckman, K. Khosoussi, N. Kottege, B. Morrell, M. Hutter, F. Pauling, F. Pomerleau, M. Saska, S. Scherer, R. Siegwart, J. L. Williams, and L. Carlone, "Present and Future of SLAM in Extreme Environments: The DARPA SubT Challenge," *IEEE Transactions on Robotics*, vol. 40, pp. 936–959, 2024.
- [8] W. Xu, Y. Cai, D. He, J. Lin, and F. Zhang, "FAST-LIO2: Fast Direct LiDAR-Inertial Odometry," *IEEE Transactions on Robotics*, vol. 38, no. 4, pp. 2053–2073, 2022.
- [9] A. Reinke, M. Palieri, B. Morrell, Y. Chang, K. Ebadi, L. Carlone, and A.-a. Agha-Mohammadi, "LOCUS 2.0: Robust and Computationally Efficient Lidar Odometry for Real-Time 3D Mapping," *IEEE Robotics and Automation Letters*, vol. 7, no. 4, pp. 9043–9050, 2022.
- [10] H. Yin, X. Xu, S. Lu, X. Chen, R. Xiong, S. Shen, C. Stachniss, and Y. Wang, "A Survey on Global LiDAR Localization: Challenges, Advances and Open Problems," *International Journal of Computer Vision*, vol. 132, no. 8, pp. 3139–3171, Aug 2024.
- [11] S. Lowry, N. Sünderhauf, P. Newman, J. J. Leonard, D. Cox, P. Corke, and M. J. Milford, "Visual Place Recognition: A Survey," *IEEE Transactions on Robotics*, vol. 32, no. 1, pp. 1–19, 2016.
- [12] S. Schubert, P. Neubert, S. Garg, M. Milford, and T. Fischer, "Visual Place Recognition: A Tutorial [Tutorial]," *IEEE Robotics & Automation Magazine*, vol. 31, no. 3, pp. 139–153, 2024.
- [13] P. Yin, S. Zhao, H. Lai, R. Ge, J. Zhang, H. Choset, and S. Scherer, "AutoMerge: A Framework for Map Assembling and Smoothing in City-Scale Environments," *IEEE Transactions on Robotics*, vol. 39, no. 5, pp. 3686–3704, 2023.
- [14] P. Yin, J. Jiao, S. Zhao, L. Xu, G. Huang, H. Choset, S. Scherer, and J. Han, "General Place Recognition Survey: Towards Real-World Autonomy," 2024.
- [15] N. Stathoulopoulos, M. A. Saucedo, A. Koval, and G. Nikolakopoulos, "RecNet: An Invertible Point Cloud Encoding through Range Image Embeddings for Multi-Robot Map Sharing and Reconstruction," in *2024 IEEE International Conference on Robotics and Automation (ICRA)*, 2024, pp. 4883–4889.
- [16] G. Damigos, N. Stathoulopoulos, A. Koval, T. Lindgren, and G. Nikolakopoulos, "Communication-Aware Control of Large Data Transmissions via Centralized Cognition and 5G Networks for Multi-Robot Map merging," *Journal of Intelligent & Robotic Systems*, vol. 110, no. 1, p. 22, Jan 2024.
- [17] Y. Tian, Y. Chang, F. Herrera Arias, C. Nieto-Granda, J. P. How, and L. Carlone, "Kimera-Multi: Robust, Distributed, Dense Metric-Semantic SLAM for Multi-Robot Systems," *IEEE Transactions on Robotics*, vol. 38, no. 4, pp. 2022–2038, 2022.
- [18] E. Garcia-Fidalgo and A. Ortiz, "Hierarchical Place Recognition for Topological Mapping," *IEEE Transactions on Robotics*, vol. 33, no. 5, pp. 1061–1074, 2017.
- [19] T. Shan, B. Englot, D. Meyers, W. Wang, C. Ratti, and R. Daniela, "LIO-SAM: Tightly-coupled Lidar Inertial Odometry via Smoothing and Mapping," in *IEEE/RSJ International Conference on Intelligent Robots and Systems (IROS)*. IEEE, 2020, pp. 5135–5142.
- [20] Y. Huang, T. Shan, F. Chen, and B. Englot, "DiSCO-SLAM: Distributed Scan Context-Enabled Multi-Robot LiDAR SLAM with Two-Stage Global-Local Graph Optimization," *IEEE Robotics and Automation Letters*, vol. 7, no. 2, pp. 1150–1157, 2022.
- [21] H. Gao, Q. Qiu, S. Zhang, W. Hua, Z. Su, and X. Zhang, "MPC-MF: Multi-Point Cloud Map Fusion Based on Offline Global Optimization for Mobile Robots," *Chinese Control Conference, CCC*, vol. 2023-July, pp. 4237–4242, 2023.
- [22] P. Liu, S. Bao, L. Du, J. Yuan, H. Zhang, and R. Luo, "ECH: An Enhanced Cart Histogram for place recognition," *2023 IEEE*

- International Conference on Robotics and Biomimetics (ROBIO)*, pp. 1–6, 2023.
- [23] K. Ebadi, Y. Chang, M. Palieri, A. Stephens, A. Hatteland, E. Heiden, A. Thakur, N. Funabiki, B. Morrell, S. Wood, L. Carlone, and A. A. Agha-Mohammadi, “LAMP: Large-Scale Autonomous Mapping and Positioning for Exploration of Perceptually-Degraded Subterranean Environments,” pp. 80–86, 2020.
- [24] C. Denniston, Y. Chang, A. Reinke, K. Ebadi, G. S. Sukhatme, L. Carlone, B. Morrell, and A. Akbar Agha-mohammadi, “Loop Closure Prioritization for Efficient and Scalable Multi-Robot SLAM,” *IEEE Robotics and Automation Letters*, vol. 7, pp. 9651–9658, 2022.
- [25] I. Alonso, L. Riazuelo, and A. C. Murillo, “Enhancing V-SLAM keyframe selection with an efficient convnet for semantic analysis,” in *2019 IEEE International Conference on Robotics and Automation (ICRA)*, 2019, pp. 4717–4723.
- [26] Y. Zhang, F. Tosi, S. Mattoccia, and M. Poggi, “GO-SLAM: Global Optimization for Consistent 3D Instant Reconstruction,” *2023 IEEE/CVF International Conference on Computer Vision (ICCV)*, no. ICCV, pp. 3704–3714, 2023.
- [27] H. Y. Lin and J. L. Hsu, “A Sparse Visual Odometry Technique Based on Pose Adjustment with Keyframe Matching,” *IEEE Sensors Journal*, vol. 21, no. 10, pp. 11 810–11 821, 2021.
- [28] W. Chen, L. Zhu, X. Lin, L. He, Y. Guan, and H. Zhang, “Dynamic Strategy of Keyframe Selection with PD Controller for VSLAM Systems,” *IEEE/ASME Transactions on Mechatronics*, vol. 27, no. 1, pp. 115–125, 2022.
- [29] S. Leutenegger, P. T. Furgale, V. Rabaud, M. Chli, K. Konolige, and R. Y. Siegwart, “Keyframe-Based Visual-Inertial SLAM using Nonlinear Optimization,” in *Robotics: Science and Systems*, 2013.
- [30] T. Qin, P. Li, and S. Shen, “Relocalization, Global Optimization and Map Merging for Monocular Visual-Inertial SLAM,” in *2018 IEEE International Conference on Robotics and Automation (ICRA)*, 2018, pp. 1197–1204.
- [31] X. Tao, B. Zhu, S. Xuan, J. Zhao, H. Jiang, J. Du, and W. Deng, “A Multi-Sensor Fusion Positioning Strategy for Intelligent Vehicles Using Global Pose Graph Optimization,” *IEEE Transactions on Vehicular Technology*, vol. 71, no. 3, pp. 2614–2627, 2022.
- [32] B. Kim, C. Jung, D. H. Shim, and A. Agha-mohammadi, “Adaptive Keyframe Generation based LiDAR Inertial Odometry for Complex Underground Environments,” in *2023 IEEE International Conference on Robotics and Automation (ICRA)*, 2023, pp. 3332–3338.
- [33] K. Chen, B. T. Lopez, A.-a. Agha-mohammadi, and A. Mehta, “Direct LiDAR Odometry: Fast Localization With Dense Point Clouds,” *IEEE Robotics and Automation Letters*, vol. 7, no. 2, pp. 2000–2007, 2022.
- [34] Q. Zeng, D. Liu, Y. Zhou, and Y. Peng, “Entropy-based Keyframe Established and Accelerated Fast LiDAR Odometry and Mapping,” *ITOE 2023 - IEEE 7th Information Technology and Mechatronics Engineering Conference*, vol. 7, pp. 347–354, 2023.
- [35] F. Ou, Y. Li, Z. Miao, and J. Zhou, “Lidar Odometry Key Frame Selection Based on Displacement Vector Similarity,” *Chinese Control Conference, CCC*, vol. 2021-July, pp. 3588–3593, 2021.
- [36] Y. Cui, Q. Wu, Y. Hao, Y. Kong, Z. Lin, and F. Zhu, “Fast Relocalization and Loop Closing in Keyframe-Based 3D LiDAR SLAM,” *2022 IEEE International Conference on Robotics and Biomimetics, ROBIO 2022*, pp. 590–595, 2022.
- [37] Y. Cui, X. Chen, Y. Zhang, J. Dong, Q. Wu, and F. Zhu, “BoW3D: Bag of Words for Real-Time Loop Closing in 3D LiDAR SLAM,” *IEEE Robotics and Automation Letters*, vol. 8, no. 5, pp. 2828–2835, 2023.
- [38] Y. Cui, Y. Zhang, J. Dong, H. Sun, X. Chen, and F. Zhu, “LinK3D: Linear Keypoints Representation for 3D LiDAR Point Cloud,” *IEEE Robotics and Automation Letters*, vol. 9, no. 3, pp. 2128–2135, 2024.
- [39] N. Stathoulopoulos, B. Lindqvist, A. Koval, A.-A. Agha-Mohammadi, and G. Nikolakopoulos, “FRAME: A Modular Framework for Autonomous Map Merging: Advancements in the Field,” *IEEE Transactions on Field Robotics*, vol. 1, pp. 1–26, 2024.
- [40] M. Bosse, G. Agamennoni, and I. Gilitschenski, “Robust Estimation and Applications in Robotics,” *Foundations and Trends® in Robotics*, vol. 4, no. 4, pp. 225–269, 2016.
- [41] J. Ma, J. Zhang, J. Xu, R. Ai, W. Gu, and X. Chen, “OverlapTransformer: An Efficient and Yaw-Angle-Invariant Transformer Network for LiDAR-Based Place Recognition,” *IEEE Robotics and Automation Letters*, vol. 7, no. 3, pp. 6958–6965, 2022.
- [42] J. Komorowski, M. Wysoczanska, and T. Trzcinski, “EgoNN: Egocentric Neural Network for Point Cloud Based 6DoF Relocalization at the City Scale,” *IEEE Robotics and Automation Letters*, vol. 7, no. 2, pp. 722–729, 2022.
- [43] C. Yuan, J. Lin, Z. Liu, H. Wei, X. Hong, and F. Zhang, “BTC: A Binary and Triangle Combined Descriptor for 3-D Place Recognition,” *IEEE Transactions on Robotics*, vol. 40, pp. 1580–1599, 2024.
- [44] G. Kim, S. Choi, and A. Kim, “Scan Context++: Structural Place Recognition Robust to Rotation and Lateral Variations in Urban Environments,” *IEEE Transactions on Robotics*, vol. 38, no. 3, pp. 1856–1874, 2022.
- [45] P.-Y. Lajoie, S. Hu, G. Beltrame, and L. Carlone, “Modeling Perceptual Aliasing in SLAM via Discrete–Continuous Graphical Models,” *IEEE Robotics and Automation Letters*, vol. 4, no. 2, pp. 1232–1239, 2019.
- [46] L. Schaupp, M. Bürki, R. Dubé, R. Siegwart, and C. Cadena, “OREOS: Oriented Recognition of 3D Point Clouds in Outdoor Scenarios,” in *2019 IEEE/RSJ International Conference on Intelligent Robots and Systems (IROS)*, 2019, pp. 3255–3261.
- [47] R. B. Rusu, N. Blodow, Z. C. Marton, and M. Beetz, “Aligning point cloud views using Persistent Feature Histograms,” in *2008 IEEE/RSJ International Conference on Intelligent Robots and Systems*, 2008, pp. 3384–3391.
- [48] S. Salti, F. Tombari, and L. Di Stefano, “SHOT: Unique signatures of histograms for surface and texture description,” *Computer Vision and Image Understanding*, vol. 125, pp. 251–264, 2014.
- [49] Hecht-Nielsen, “Theory of the backpropagation neural network,” in *International 1989 Joint Conference on Neural Networks*, 1989, pp. 593–605 vol.1.
- [50] A. Geiger, P. Lenz, and R. Urtasun, “Are we ready for Autonomous Driving? The KITTI Vision Benchmark Suite,” in *Conference on Computer Vision and Pattern Recognition (CVPR)*, 2012.
- [51] W. Lu, Y. Zhou, G. Wan, S. Hou, and S. Song, “L3-Net: Towards Learning Based LiDAR Localization for Autonomous Driving,” in *2019 IEEE/CVF Conference on Computer Vision and Pattern Recognition (CVPR)*, 2019, pp. 6382–6391.
- [52] G. Kim, Y. S. Park, Y. Cho, J. Jeong, and A. Kim, “MulRan: Multimodal Range Dataset for Urban Place Recognition,” in *2020 IEEE International Conference on Robotics and Automation (ICRA)*, 2020, pp. 6246–6253.
- [53] G. Pandey, J. R. McBride, and R. M. Eustice, “Ford Campus vision and lidar data set,” *The International Journal of Robotics Research*, vol. 30, no. 13, pp. 1543–1552, 2011.
- [54] G. Kim and A. Kim, “Scan Context: Egocentric Spatial Descriptor for Place Recognition Within 3D Point Cloud Map,” in *2018 IEEE/RSJ International Conference on Intelligent Robots and Systems (IROS)*, 2018, pp. 4802–4809.
- [55] L. van der Maaten and G. Hinton, “Visualizing Data using t-SNE,” *Journal of Machine Learning Research*, vol. 9, no. 86, pp. 2579–2605, 2008.